Human Serum is a Potent Chemoattractant for Enterobacteriaceae Species Associated with Gastrointestinal Bleeding

Siena J. Glenn[1□], Zealon Gentry-Lear[2□], Michael Shavlik[2], Michael J. Harms[2,3], Thomas J. Asaki[4], and Arden Baylink[1*]

[1] Washington State University, Department of Veterinary Microbiology and Pathology, Pullman, WA 99164

[2] University of Oregon, Institute of Molecular Biology, Eugene, OR, 97403

[3] University of Oregon, Department of Chemistry & Biochemistry, Eugene, OR, 97403

[□] Authors contributed equally to this work.

[4] Washington State University, Department of Mathematics and Statistics, Pullman, WA 99164

[*] Corresponding author: arden.baylink@wsu.edu (A. Baylink)

Abstract

Enterobacteriaceae bacteria are prone to opportunistic pathogenic behavior during gut dysbiosis, potentially influenced by distinct environmental cues within the compromised gut. Chemosensing systems play a central role in allowing bacteria to perceive and react to physicochemical signals within the gastrointestinal (GI) milieu, influencing their motility, population organization, and colonization site preferences. We investigated the chemosensory behavior of Enterobacteriaceae, a bacterial family associated with gastrointestinal (GI) bleeding and sepsis, to learn whether these bacteria respond to human serum, a chemical stimulus they encounter during GI bleeding. We discover that clinical isolates of diverse non-typhoidal *Salmonella enterica* serovars, *Escherichia coli*, and *Citrobacter koseri* all sense human serum as a potent attractant. Using a custom injection-based microfluidics device we simulated GI bleeding and found that femtoliter volumes of human serum are sufficient to stimulate motile cells to rapidly swim toward, and congregate at, the serum source. With exceptional temporal resolution, we determined that this response is orchestrated through chemotaxis, with a major chemical cue driving chemoattraction being L-serine, an amino acid abundantly present in serum, recognized by the chemoreceptor Tsr. To gain deeper insight into the structural basis of this phenomenon, we successfully elucidated the crystal structure of *Salmonella* Typhimurium Tsr in

complex with L-serine. This structure allowed for a precise characterization of the ligand-binding site, thereby correcting prior misconceptions regarding L-serine positioning and accurately defining the chemoreceptor's ligand-binding interactions. Building upon these structural insights, we identified a conserved amino acid recognition motif for L-serine shared among Tsr orthologues and mapped the phylogenetic distribution of this chemoreceptor. We found that Tsr, which mediates serum chemoattraction, is widely conserved among Enterobacteriaceae and many World Health Organization priority pathogens associated with bloodstream infections. Given that Enterobacteriaceae are a primary cause of bacteremia and sepsis, particularly as a complication of inflammatory bowel diseases, their remarkable sensitivity to serum as a chemoattractant could relate to their proclivity for bloodstream entry.

Introduction

Bacteria use chemosensory systems to survey and navigate their environments [1–3]. In the exceptionally dynamic environment of the host gut, peristalsis and flow constantly perturb the microscopic physicochemical landscape. Key to responding to such transient and shifting stimuli is that chemosensing allows bacteria to rapidly restructure their populations, within seconds, to be attracted toward, or repelled away from, effector sources [4–6]. Enteric pathogens and pathobionts use chemosensing to colonize specific tissues, based on sources of exogenous nutrients, toxins, and host-emitted cues, through control of motility and adhesion systems such as chemotaxis, chemokinesis, twitching, and biofilm formation [3,7–11]. Notably, most bacterial genera classified by the World Health Organization (WHO) as ‘priority pathogens’ employ sophisticated chemosensory systems for efficient infection and exert precise control over their colonization topography [3,12,13]. These include multidrug-resistant Enterobacteriaceae pathogens of the gut such as *Salmonella enterica*, Enterohemorrhagic *Escherichia coli* (EHEC), *Citrobacter koseri*, and *Enterobacter cloacae*, which present major challenges for nosocomial infections and global health [3,13].

The signals that enteric bacteria perceive through chemosensing are most comprehensively understood in the context of colonizing of a healthy gut, a state referred to as eubiosis. These signals include host-emitted amino acids indicating proximity to a host [14], quorum-sensing molecules from the microbiome that convey intra- and inter-species information [15], and urea emanating from tissue that direct bacteria out of the lumen and into contact with the

epithelia [5]. However, gut dysbiosis, induced by pathologies, inflammation, and infections, exposes enteric bacteria to novel and distinct chemical stimuli that may drive their behavior towards opportunistic pathogenesis [3,16]. While it is well-established that bacterial chemosensing enhances colonization and persistence within the gut [3], our understanding of which host-emitted cues are responded to by pathogens and pathobionts in the diseased and compromised gut remains limited. Furthermore, most studies on bacterial chemosensing employ assays that neglect the rapid temporal dimension fundamental to how these responses confer advantages in the dynamic gut environment. Investigating how chemosensing governs the swift responses of pathogen populations to unique chemical features associated with dysbiosis presents an opportunity to gain deeper insights into bacterial behaviors that influence the critical juncture between infection resolution and exacerbation (Fig. 1) [3,16–18].

In a diseased gut, enteric bacteria may encounter a distinctive host-derived chemical feature not found in a healthy gut – GI bleeding. The microenvironment of an enteric hemorrhagic lesion involves a source of serum, the liquid component of blood, emanating from the host tissue and diffusing into the intestinal lumen (Fig. 1). In effect, this creates a microscopic gradient, i.e., a microgradient, of chemicals flowing outward from a point source that may serve as chemosensory signals for luminal bacteria. Enteric infections caused by Enterobacteriaceae species can lead to GI bleeding, a condition associated with a significant risk of mortality. Although GI bleeding isn't a typical outcome of enteric infection, it is a substantial burden on human health, affecting around 40-150 out of every 100,000 individuals annually, with a fatality rate ranging from 6% to 30% of cases (Fig. 1) [3,13,19–21,21–24]. Notably, Enterobacteriaceae are prone to bloodstream entry, and are a leading cause of sepsis-related deaths in individuals with inflammatory bowel diseases (IBD) [25,26]. Despite the established connection between Enterobacteriaceae virulence and GI bleeding, it remained unknown whether these bacteria perceive serum through chemosensing.

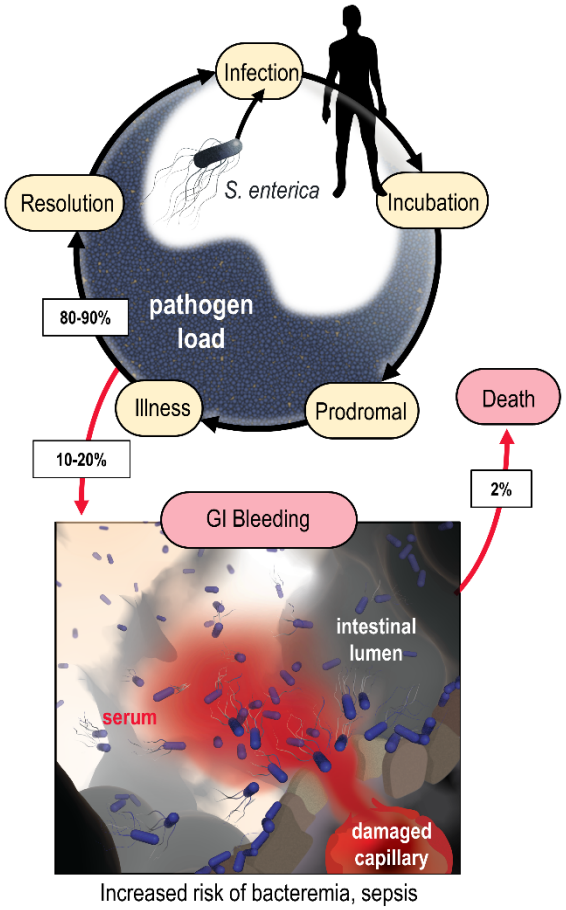

Fig. 1. Model of the microenvironment of bacterial-induced hemorrhagic lesions. The typical course of non-typhoidal *S. enterica* infections is shown proceeding through infection, incubation, prodromal, illness, and resolution stages (black arrows). The atypical route of GI bleeding, associated with increased mortality and morbidity, is shown in red arrows, with rates approximated from available literature. An artistic depiction of bacterial injury tropism is shown bottom.

Serum is a complex biological solution with components that may enhance, or hinder, bacterial growth. On one hand, it offers a rich reservoir of nutrients for bacteria: sugars and amino acids at millimolar concentrations [3,27]. Additionally, it contains essential metals like iron and zinc. On the other hand, serum contains host factors that inhibit bacterial proliferation in the bloodstream such as cathelicidin, defensins, and the complement system [28,29]. Consequently, how enteric pathogens and pathobionts would respond to serum exposure remained unclear. To address this open question, we employed an injection-based live-imaging system to simulate GI bleeding with human serum *in vitro* and measure bacterial chemosensing responses with high temporal resolution. We initially focused on non-typhoidal serovars of the human enteric pathogen *S. enterica* as exemplars of Enterobacteriaceae that can cause GI hemorrhaging and sepsis (Fig. 1). These serovars are responsible for approximately 1.35 million infections each year and possess chemosensory systems characteristic of Enterobacteriaceae [3,30]. Subsequently,

we studied the chemosensing responses of the Enterobacteriaceae species *E. coli* and *C. koseri* to human serum. Across all examined scenarios, we observe these bacteria to exhibit a remarkable sensitivity and attraction towards human serum. This phenomenon is an example of how stimuli unique to the environment of a diseased gut may promote, through chemosensing, emergent bacterial behaviors that can adversely impact host health, and may relate to the propensity of Enterobacteriaceae to invade the bloodstream.

Results

Use of the chemosensory injection rig assay (CIRA) to study polymicrobial chemosensing behaviors

To model features of enteric bleeding *in vitro*, we utilized an experimental system to inject minute quantities of human serum into a pond of motile bacteria and observe real-time responses by microscopy (Fig. 2A). The system and methodology, which we refer to herein as the chemosensory injection rig assay (CIRA), offers several advantages for studying bacterial chemosensing and localization in response to serum: (1) we can use bona fide human serum, (2) the readouts are direct measurements of real-time localization dynamics of the bacterial population, and (3) similar to a bleeding event, a source of fresh serum is continuously emitted. By employing multichannel fluorescence imaging of differentially labeled bacterial populations we observe polymicrobial interactions through head-to-head comparisons of bacterial behavior within the same experiment.

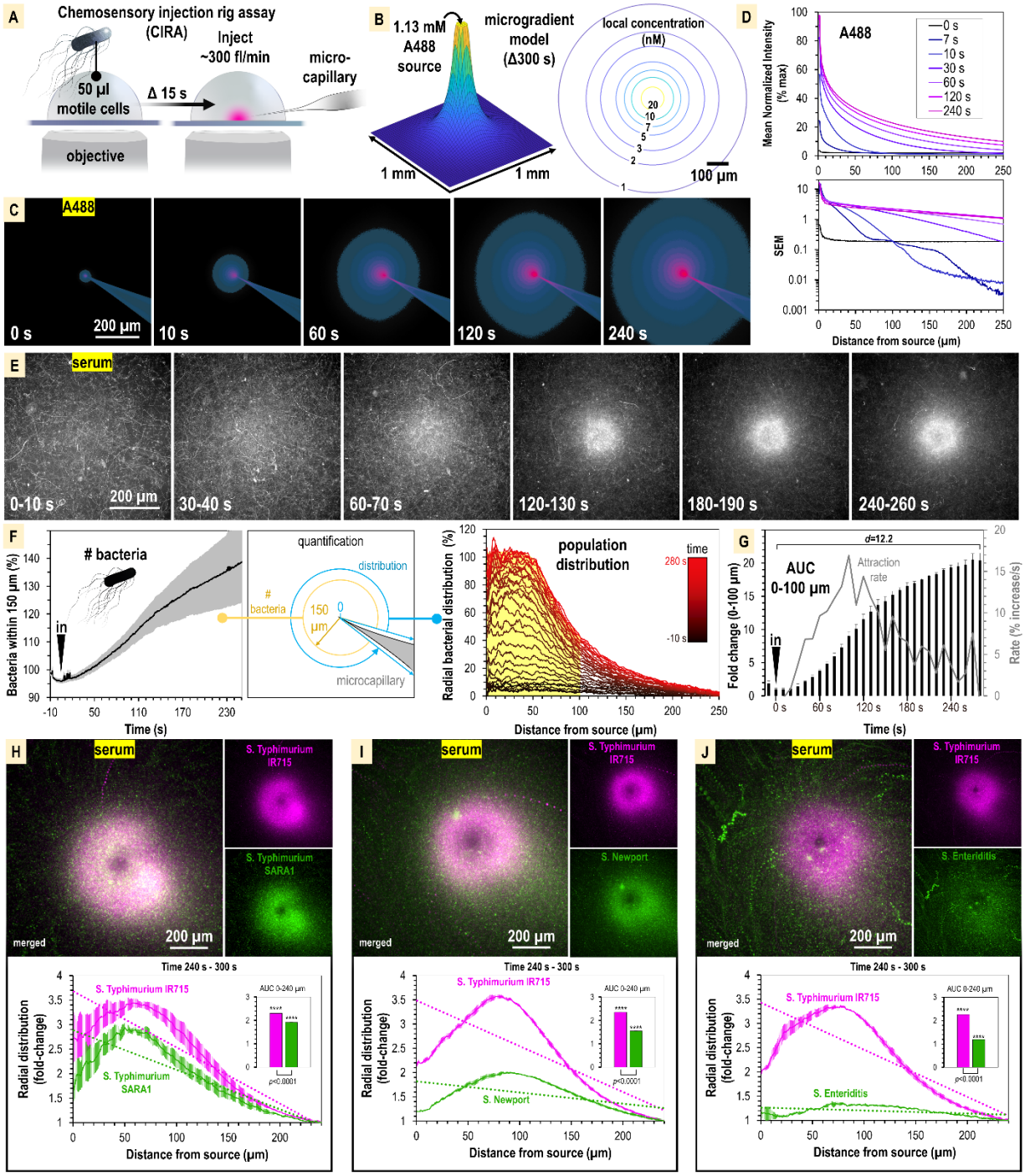
A
Chemosensory injection rig assay (CIRA)
Inject ~300 fl/min
micro-capillary
50 µl motile cells
Δ 15 s
objective
B
1.13 mM A488 source
microgradient model (Δ300 s)
local concentration (nM)
1 mm
1 mm
100 µm
C
A488
0 s
200 µm
10 s
60 s
120 s
240 s
D
A488
Mean Normalized Intensity (% max)
0 s
7 s
10 s
30 s
60 s
120 s
240 s
SEM
Distance from source (µm)
E
serum
0-10 s
200 µm
30-40 s
60-70 s
120-130 s
180-190 s
240-260 s
F
bacteria
Bacteria within 150 µm (%)
in
Time (s)
quantification
distribution
bacteria
150 µm
microcapillary
Radial bacterial distribution (%)
population distribution
time
280 s
-10 s
Distance from source (µm)
G
d=12.2
AUC 0-100 µm
Attraction rate
Fold change (0-100 µm)
Rate (% increase/s)
in
Time (s)
H
serum
S. Typhimurium IR715
S. Typhimurium SARA1
merged
200 µm
Time 240 s - 300 s
Radial distribution (fold-change)
AUC 0-240 µm
p<0.0001
Distance from source (µm)
I
serum
S. Typhimurium IR715
S. Newport
merged
200 µm
Time 240 s - 300 s
Radial distribution (fold-change)
AUC 0-240 µm
p<0.0001
Distance from source (µm)
J
serum
S. Typhimurium IR715
S. Enteriditis
merged
200 µm
Time 240 s - 300 s
Radial distribution (fold-change)
AUC 0-240 µm
p<0.0001
Distance from source (µm)

Fig. 2. *S. enterica* serovars rapidly localize toward human serum. A. CIRA experimental design. B. CIRA microgradient model, simulated with a source of 1.13 mM A488 dye after 300 s of injection. C. Visualization of the CIRA microgradient with A488 dye. D. Radial distribution of A488 dye at representative time points (n=6). E. Response of *S. enterica* Typhimurium IR715 to human serum (max projections over 10 s intervals). F. Quantification of *S. enterica* Typhimurium IR715 attraction response to human serum (n=4, 37˚ C) characterized as either the relative number of bacteria within 150 µM of the source (left), or the radial distribution of the bacterial population over time (right, shown in 10 s intervals). G. Area under the curve (AUC) versus time for the bacterial population within 100 µm of the serum treatment source (area indicated in yellow in panel F). Effect size (Cohen's *d*) between the treatment start and endpoints is indicated. Insertion of the treatment microcapillary is indicated with black arrow. Attraction rate over time indicated in gray. H-J. CIRA competition experiments between *S.* Typhimurium IR715 (pink) and clinical isolates (green) responding to human serum for 5 mins (n=4, 37˚ C). Images are representative max projections over the final minute of treatment. Radial distributions calculated from max projections and averaged across replicates are shown as fold-change relative to the image periphery at 240 µm from the source. Inset plots show fold-change AUC of strains in the same experiment, with *p*-values from unpaired two-sided t-test, or one-sided t-test (stars) relative to an expected baseline of 1. Trend lines (dashed) indicate the degree of bias in the population distribution, with increasingly negative slope reflecting greater chemoattraction. Data shown are means, error bars indicate SEM. See also Fig. S1, Table S1, Movie S1,

The CIRA microgradient is established through injection at a constant rate of ~300 femtoliters per minute, through a 0.5 µm glass microcapillary, and expands over time from diffusion (Fig. 2A-B, Fig. S1). To approximate the diffusion of serum metabolites we developed a mathematical model for the CIRA microgradient based on the three-dimensional differential diffusion equation (Fig. 2B, Fig. S1, Method Details). From this model, we calculate that the introduction of a minute volume of novel effector produces a steep microgradient, in which a millimolar source recedes to nanomolar concentrations after diffusion across only a few hundred microns (Fig. 2B, Fig. S1). For instance, we expect a bacterium 100 µm from a 1 mM infinite-volume source to experience a local concentration of a small molecule effector (diffusion coefficient approximately 4×10^{-6} cm^2 s^{-1}) of 10 nM after 300 s of injection (Fig. 2B, Fig. S1). To visualize the microgradient experimentally, we utilized Alexa Fluor 488 dye (A488) and observed the microgradient to be stable and consistent across replicates (Fig. 2C-D, Movie S1). We found no behavioral differences in treatments with buffer in the range of pH 4-9, indicating small, localized pH changes are inconsequential for taxis in our system, and that any artifactual forces, such as flow, account for only minor changes to bacterial distribution at the population level, in the range of ±10% (Fig. S1).

Non-typhoidal S. enterica serovars exhibit rapid attraction to human serum

We first studied the chemosensing behaviors of *S.* Typhimurium IR715, which is a derivative of ATCC 14028, originally isolated from domesticated chickens, and is used extensively in the study of *Salmonella* pathogenesis (Table S1)[31–34]. As treatment, we utilized commercially-available human serum that was not heat-inactivated nor exposed to chemical or physical treatments that would be expected to alter its native complement properties (see Materials & Methods). We assessed the response of motile IR715, containing a fluorescent mPlum marker, to a source of human serum over the course of 5 minutes (Fig. 2E, Movie S1). During this timeframe, we witnessed a rapid attraction response whereby the motile bacterial population reorganized from a random distribution to one concentrated within a 100-150 µm radius of the serum source (Fig. 2E-F, Movie S1). To compare responses between CIRA experiments, we plotted data as either the relative number of bacteria within 150 µm of the treatment (Fig. 2F, left panel) or a radial distribution of the population (Fig. 2F, right panel) over time. By these measures we determined *S.* Typhimurium IR715 is attracted to human serum. The bacterial population in proximity to the serum source doubles by 40 s, reaches a maximal attraction rate by 90 s, and approaches equilibrium by 300 s post-treatment (Fig. 2G).

To test whether serum attraction is relevant for *Salmonella* strains that infect humans, and if responses differ among non-typhoidal *Salmonella* serovars, we employed dual-channel CIRA imaging to compete *S.* Typhimurium IR715 against representative clinical isolates of Typhimurium (SARA1), Newport (M11018046001A), and Enteriditis (05E01375). These serovars are the most common in North American infections [35]. In varying magnitude, all strains showed attraction responses to human serum, seen as a significant distribution bias toward the serum source relative to the experiment periphery (Fig. 2H-J, Movie S2). Together, our data show *S. enterica* serovars that cause disease in humans are exquisitely sensitive to human serum, responding to femtoliter quantities as an attractant, and that distinct reorganization at the population level occurs within minutes of exposure (Fig. 2H-J, Movie S2).

Chemotaxis and the chemoreceptor Tsr mediate serum attraction

Serum is a complex biological solution containing a variety of sugars, amino acids, and other metabolites that could serve as attractant signals [3]. Based on the rapid attraction of motile, swimming bacteria to the treatment source, characteristic of chemotactic behaviors [5], we

hypothesized serum to be perceived through the chemotaxis system, and that one or more of these chemical components could be specifically recognized as chemoattractants through the repertoire of chemoreceptors possessed by *Salmonellae* (Fig. 3A). Based on current understanding of chemoreceptor-chemoattractant ligand interactions [3,36], we identified three chemoreceptors that could mediate serum chemoattraction: (1) taxis to serine and repellents (Tsr), which responds to L-serine, and reportedly also norepinephrine (NE) and 3,4-dihydroxymandelic acid (DHMA); (2) taxis to ribose and glucose/galactose (Trg), which responds to glucose and galactose; and (3) taxis to aspartate and repellents (Tar), which responds to L-aspartate (Fig. 3A). We modeled the local concentration profile of these effectors based on their typical concentrations in human serum (Fig. 3B). The two most prevalent chemoattractants in serum are glucose (5 mM) and L-serine (100-300 μM) (Fig. 3B-F), which suggested the chemoreceptors Trg and/or Tsr could mediate serum attraction. These chemoreceptors were shown previously to be important for infection and survival during colitis [34].

To test the role of chemotaxis in serum attraction, we competed wildtype (WT) *S.* Typhimurium IR715 against a chemotaxis-null isogenic *cheY* mutant, which possesses swimming motility but is blind to chemoeffector signals (Fig. 3G, Movie S3). Whereas the WT mounts a robust attraction response to serum, the *cheY* mutant population remains randomly distributed (Fig. 3G, Movie S3). We also observed the *cheY* mutant to exhibit a slight decline in cells proximal to the treatment source over time, which we attribute to cellular crowding effects from the influx of WT cells (Fig. 3G, Movie S3). In this background, the fraction of WT cells within 100 μm of the serum source increases by 70-fold, with maximal rate of attraction achieved by 120 s post treatment. Thus, we determined that chemotaxis, i.e., chemoattraction, is namely responsible for the rapid localization of *S. enterica* to human serum.

We next analyzed strains with deletions of the chemoreceptors *trg*, or *tsr*, to test the roles of these chemoreceptors in mediating serum chemoattraction. Surprisingly, we found the *trg* strain to be non-motile (data not shown). Because motility is a prerequisite for chemotaxis, we chose not to study the *trg* mutant further, and instead focused our mechanistic investigations on Tsr. We compared chemoattraction responses in dual-channel CIRA experiments between the WT and *tsr* mutant and observed an interesting behavior whereby both strains exhibited chemoattraction, but the *tsr* mutant distribution was relegated to a halo at the periphery of the WT peak (Fig. 3H, Movie S3). The WT efficiently outcompetes the *tsr* mutant such that by 5

minutes post-treatment the ratio of WT to *tsr* cells proximal to the serum source is 3:1 (Fig. 3H, Movie S3). Similar to *cheY*, we presume the *tsr* halo results from cellular crowding effects induced by the high density of WT cells near the serum source. To test how the *tsr* mutant responds to serum in the absence of a strong competitor, we compared chemoattraction between *tsr* and *cheY*. In this background, *tsr* chemoattraction remained diminished relative to that of WT, but the *tsr* distribution shifted closer to the serum source (Fig. 3I, Movie S3). These results led us to conclude that the mechanism underlying serum chemoattraction involves the chemoreceptor Tsr and acts through one, or more, of the chemoattractants recognized by Tsr that is present in serum: L-serine, NE, or DHMA.

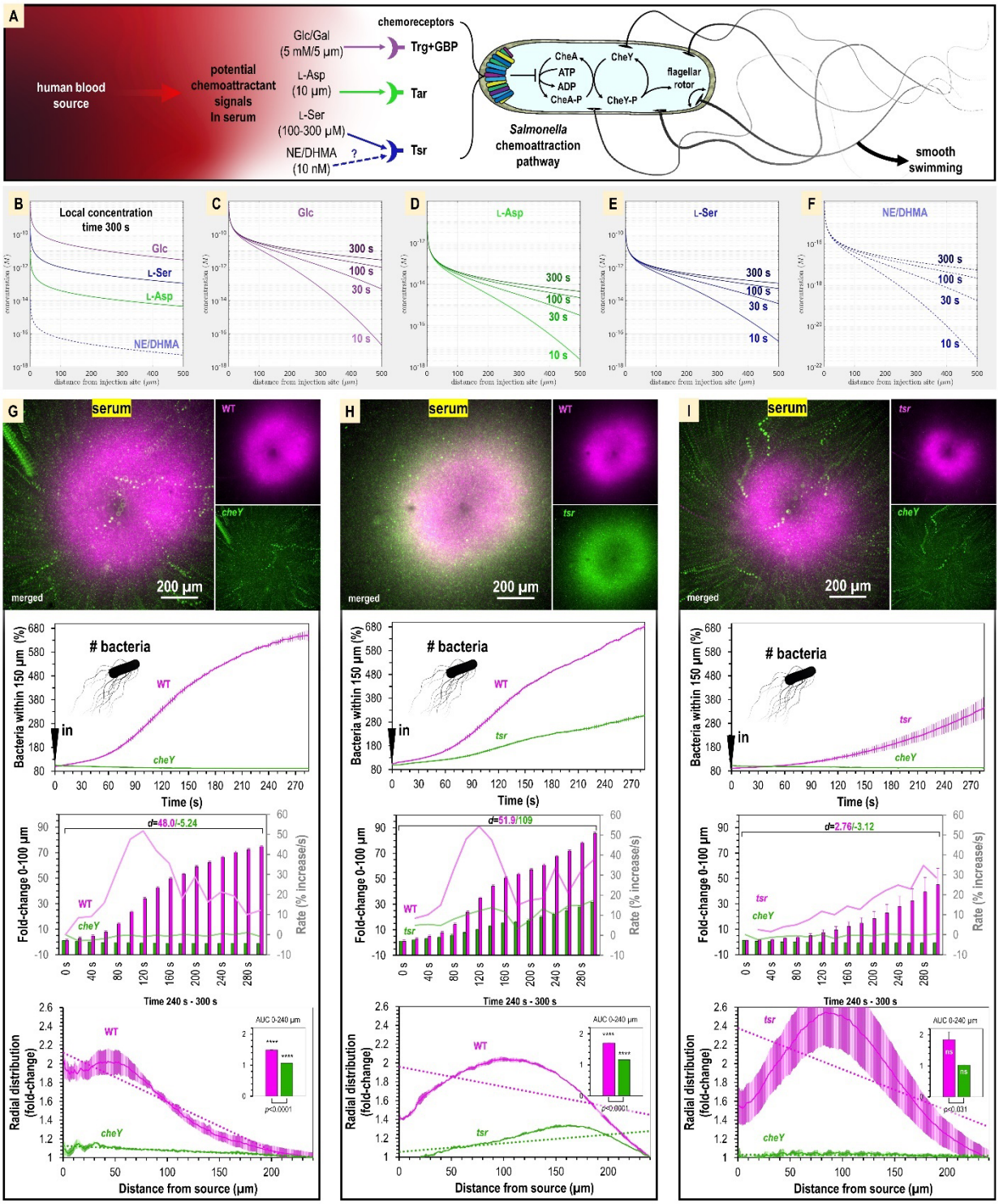
A
human blood source
potential chemoattractant signals in serum
Glc/Gal (5 mM/5 µM)
L-Asp (10 µM)
L-Ser (100-300 µM)
NE/DHMA (10 nM)
chemoreceptors
Trg+GBP
Tar
Tsr
CheA
CheY
ATP
ADP
CheA-P
CheY-P
flagellar rotor
Salmonella chemoattraction pathway
smooth swimming
B
Local concentration time 300 s
Glc
L-Ser
L-Asp
NE/DHMA
C
Glc
D
L-Asp
E
L-Ser
F
NE/DHMA
300 s
100 s
30 s
10 s
distance from injection site (µm)
G
serum
WT
cheY
merged
200 µm
H
serum
WT
tsr
merged
200 µm
I
serum
tsr
cheY
merged
200 µm
bacteria
in
Bacteria within 150 µm (%)
Time (s)
d=48.0/-5.24
d=51.9/109
d=2.76/-3.12
Fold-change 0-100 µm
Rate (% increase/s)
Time 240 s - 300 s
AUC 0-240 µm
p<0.0001
p<0.031
ns
Radial distribution (fold-change)
Distance from source (µm)

Fig. 3. Attraction to human serum is mediated through chemotaxis and the chemoreceptor Tsr. A. Potential mechanisms involved in *Salmonella* sensing of chemoattractants present in human serum. Approximate concentrations of these effectors in human serum are indicated in parentheses [3]. B-F. Microgradient modeling of serum chemoattractant concentrations. G-H. CIRA competition experiments between *S.* Typhimurium IR715 WT and isogenic mutants *cheY*, or *tsr*, and *tsr* versus *cheY*, in response to human serum (n=3-4, 37˚ C). Rates in terms of fold-change are indicated with light pink/light green lines and plotted on the gray secondary y-axis. Data are means and error bars are SEM. See also Table S1, Movie S3.

S. enterica exhibits chemoattraction to L-serine, but not NE or DHMA

We next sought to identify the specific chemoattractants driving Tsr-mediated serum chemoattraction. Suspecting that one effector might be L-serine, we took advantage of the fact that Tsr can only bind L-serine, and treated the serum with serine racemace, an enzyme that converts L- to D-serine. Comparing responses to serum, versus serum treated with serine racemace, showed that the latter decreased chemoattraction, with the localization of bacteria becoming more diffuse (Fig. S2). We next used CIRA to examine responses to purified effectors diluted in buffer. The concentration of L-serine in human serum ranges from approximately 100-400 µm, depending on diet and health factors [37–39], whereas the neurotransmitter NE, and its metabolized form, DHMA, are thought to circulate at approximately 10 nM [40,41]. Nevertheless, it has been proposed that NE and/or DHMA are sensed directly by Tsr with nanomolar affinity [42,43]. We used CIRA to test the response of *S. Typhimurium* IR715 to L-serine, NE, and DHMA. We observed robust chemoattraction responses to L-serine, but no detectable response to either NE or DHMA (Fig. S2, Movie S4-6). We attempted additional CIRA experiments with cells cultured according to prior work, which included culturing the cells with NE before chemotaxis experiments, but ultimately saw no evidence to suggest *S. enterica* responds chemotactically to NE or DHMA (Fig. S2, Movie S5-6). Together, these data indicate the chemoattractant in serum sensed through Tsr is L-serine.

Chemoattraction to L-serine has mostly been studied in the context of model laboratory strains and has not been rigorously evaluated for *S. enterica* clinical isolates or various serovars. To establish whether L-serine sensing is relevant for human infections, we used dual-channel CIRA to compare taxis to L-serine between *S.* Typhimurium IR715 and clinical isolates (Fig. 4A-C, Movie S4). In each case we observe robust chemoattraction, though there are differences in sensitivity to L-serine. The magnitude of chemoattraction was highest for *S.* Typhimurium

SARA1 and *S.* Newport, whereas *S.* Typhimurium IR715 and *S.* Enteriditis showed lower responses, which could relate to the different host specificities of these serovars and strains (Fig. 4A-C, Movie S4).

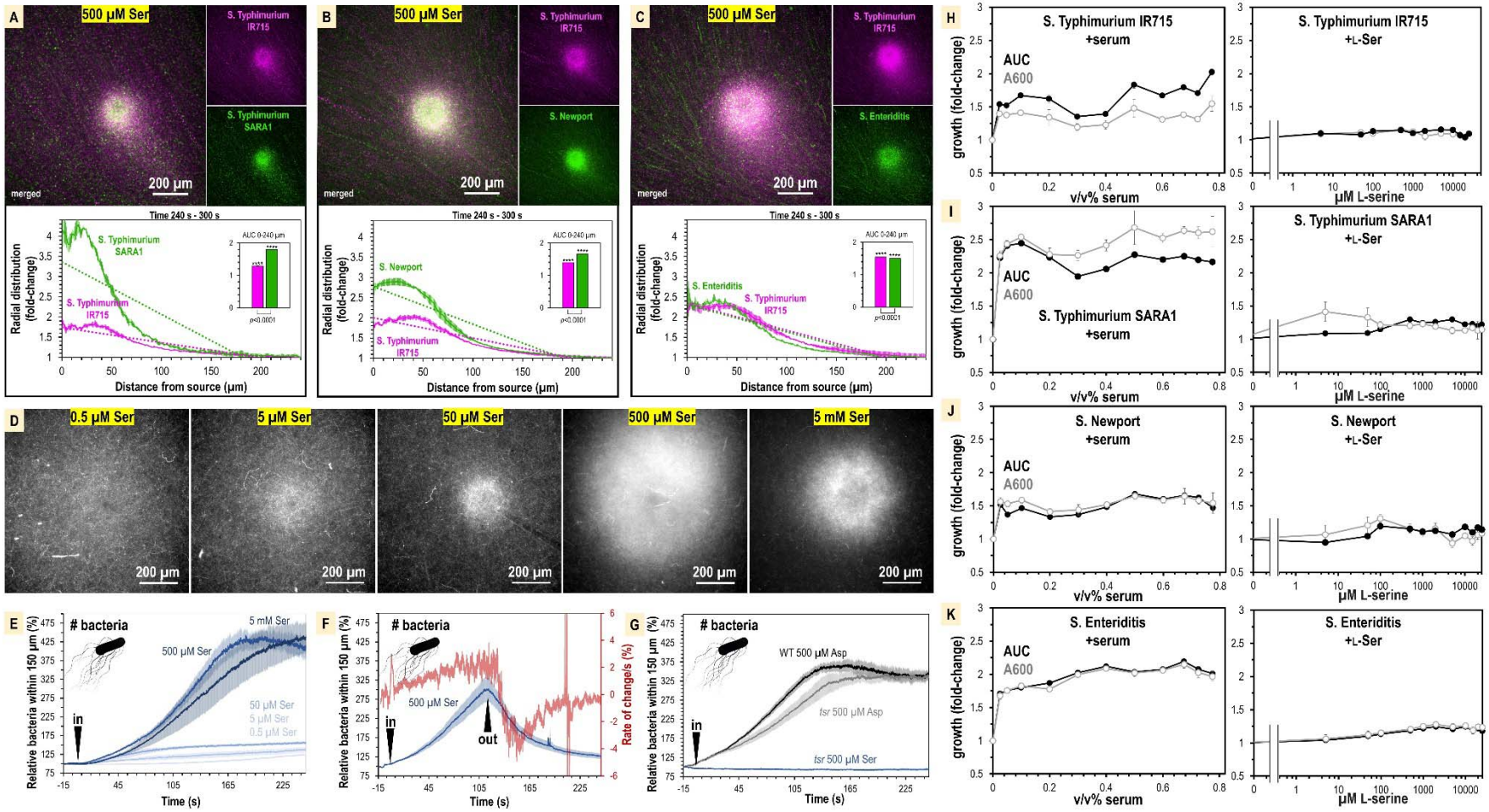
A
500 µM Ser
S. Typhimurium IR715
S. Typhimurium SARA1
merged
200 µm
Time 240 s - 300 s
Radial distribution (fold-change)
Distance from source (µm)
AUC 0-240 µm
B
S. Newport
C
S. Enteriditis
D
0.5 µM Ser
5 µM Ser
50 µM Ser
5 mM Ser
E
bacteria
Relative bacteria within 150 µm (%)
Time (s)
in
F
out
Rate of change/s (%)
G
WT 500 µM Asp
tsr 500 µM Asp
tsr 500 µM Ser
H
S. Typhimurium IR715 +serum
S. Typhimurium IR715 +L-Ser
growth (fold-change)
v/v% serum
µM L-serine
AUC
A600
I
S. Typhimurium SARA1 +serum
S. Typhimurium SARA1 +L-Ser
J
S. Newport +serum
S. Newport +L-Ser
K
S. Enteriditis +serum
S. Enteriditis +L-Ser

242

Fig. 4. L-serine is sensed as a chemoattractant molecular cue but provides little growth advantage. A-C. CIRA competition experiments between *S.* Typhimurium IR715 (pink) and clinical isolates (green) in response to 500 µM L-serine (n=3, 37˚ C). D. Representative results showing max projections of *S.* Typhimurium IR715 at 240 – 300 s post CIRA treatment with L-serine concentrations (30˚ C). E. Quantification of multiple replicate experiments shown in D. F. Attraction and dispersion of *S.* Typhimurium IR715 following addition and removal of 500 µM L-serine source (30˚ C). G. *S.* Typhimurium IR715 WT or *tsr* mutant responses to L-aspartate or L-serine treatments (30˚ C). H-I. Serum provides a growth benefit for diverse *S. enterica* serovars, that is not recapitulated by L-serine treatment alone. Growth is shown as area under the curve (AUC, black) and A600 at mid-log phase for the untreated replicates (gray, n=16). Data are means and error is SEM. See also Fig. S2, Fig. S3, Fig. S4, Movie S4, Movie S5, Movie S6.

We next used CIRA to test a range of L-serine sources spanning five orders of magnitude to define whether the concentrations of L-serine present in human serum are sufficient to drive a chemoattraction response. Within the 5 min timeframe of our experiments, the minimal source concentration of L-serine needed to induce chemoattraction is 0.5-5 µM. The [L-serine] required for half maximal chemoattraction (i.e., $K_{1/2}$) is approximately 105 µM (Fig. 4D-E, Fig. S3). Based on our microgradient modeling, this corresponds to a local L-serine concentration of 4.35 nM for bacteria 100 µm from the source (Fig. S1, Fig. 3B). To gain further insights into the dynamics of L-serine chemoattraction, we monitored chemotactic behavior in the presence of L-serine, and then removed the treatment (Fig. 4F). These experiments showed maximal attraction and dispersal rates to be similar, changing by approximately 4% per second (Fig. 4F). These findings emphasize the rapid dynamics through which chemotaxis can influence the localization of bacteria in response to microscopic gradients of chemoeffectors.

To substantiate our findings, we considered some alternative explanations for our data. First, we tested whether Tsr alone was required for chemoattraction to L-serine, or whether some other chemoreceptor, or form of taxis, such as energy or redox taxis, might contribute to the responses. However, we found when treated with L-serine, the *tsr* mutant showed no chemoattraction and behaved similarly to the chemotaxis-null *cheY* mutant (Fig. 4G). Second, we considered the possibility that the defect in serum chemoattraction of the *tsr* mutant could be due to pleiotropic effects of the *tsr* deletion on chemotaxis signaling or motility, similar to the inhibited swimming motility of the *trg* mutant. We tested the ability of the *tsr* strain to respond to another chemoattractant, L-aspartate, which is sensed through the Tar chemoreceptor (Fig. 3A). We found that the *tsr* mutant mounted a robust chemoattraction response to 500 µM L-aspartate,

similar in magnitude and rate to WT (Fig. 4G), supporting that chemotaxis to non-serine stimuli remains functional in the *tsr* strain. Together, these data support that the mechanism of Tsr-mediated chemoattraction to serum is through direct recognition of L-serine.

Serum provides a growth advantage for non-typhoidal S. enterica serovars

The robust serum chemoattraction response conserved across diverse *Salmonella* serovars suggests serum, and L-serine present in serum, could be a source of nutrients during infection. Yet, serum also contains complement proteins and bactericidal factors, such as defensins and cathelicidin, that could inhibit bacterial growth [28]. To address this, we investigated whether active human serum provides a growth benefit for *Salmonella* when diluted into minimal media. In all strains surveyed, we found that serum addition enhances growth, and we saw no evidence of killing even for the highest serum concentrations tested (Fig. 4H-K). The growth enhancement required relatively little serum, as 2.5% v/v was sufficient to provide a 1.5-2.5-fold growth increase (Fig. 4H-K).

Since L-serine is not only a chemoattractant, but also an important nutrient for bacteria in the gut [3], we hypothesized the growth benefit could be directly from L-serine. We determined by mass spectrometry that our human serum samples contain 241 µM +/- 48 total serine (L- and D-enantiomers), of which approximately 99% is expected to be L-serine [44] (Fig. S4). We attempted to treat human serum with a purified recombinant enzyme that degrades L-serine, serine dehydrogenase (SDS), to see whether serine-depleted serum would elicit less growth or chemoattraction. However, these treatments did not alter serum serine content relative to untreated samples, and so we abandoned this approach (Fig. S4). Instead, we performed a titration of purified L-serine and assessed its role in supporting a growth advantage. We found that only a very small benefit is achieved with the addition of L-serine, which did not recapitulate the larger growth benefit seen for serum addition (Fig. 4H-K). This leads us to believe that L-serine functions as a molecular cue that directs *Salmonella* toward serum, but nutrients present in serum other than L-serine provide the growth advantages.

Structure of S. enterica Tsr in complex with L-serine

We next undertook structural studies to understand the specific recognition of L-serine by Tsr. The full-length Tsr protein includes a periplasmic ligand-binding domain (LBD), a

transmembrane HAMP domain, and a cytosolic coiled-coil region, which oligomerizes to form trimers-of-dimers, and complexes with the downstream chemotaxis signaling components, CheA and CheW (Fig. 5A) [45]. No experimentally-determined structure has been published for *S. enterica* Tsr (*Se*Tsr) and the single experimentally-determined structure to have captured the L-serine-binding interactions is a crystal structure of *Ec*Tsr LBD of moderate resolution (2.5 Å, PDB: 3atp) where the electron density for the ligand is weak and the orientation of the L-serine ligand is ambiguous [46]. Despite the weakly-defined ligand interactions, this sole Tsr crystal structure has been central for use in other studies of chemoreceptor signal transduction and nanoarray function [45,47].

We recognized that in the prior *Ec*Tsr study, the methods described exchanging the protein crystal into a glycerol cryoprotectant. We hypothesized that during the glycerol soak serine leached out of the crystal leaving the binding site partially occupied, and caused the electron density to be weak for the ligand and binding region. To capture a complex with a fully-bound ligand site we grew crystals of the soluble periplasmic portion of the *Se*Tsr LBD with L-serine, at a high salt concentration that would serve as a cryoprotectant without further manipulation, and harvested crystals directly from drops so as to prevent leaching of the ligand from the binding site. Following extensive crystallization trials, we identified a single *Se*Tsr LBD crystal that diffracted to high resolution (2.2 Å) and was of sufficient quality for structure determination (Fig. 5B, Table S2).

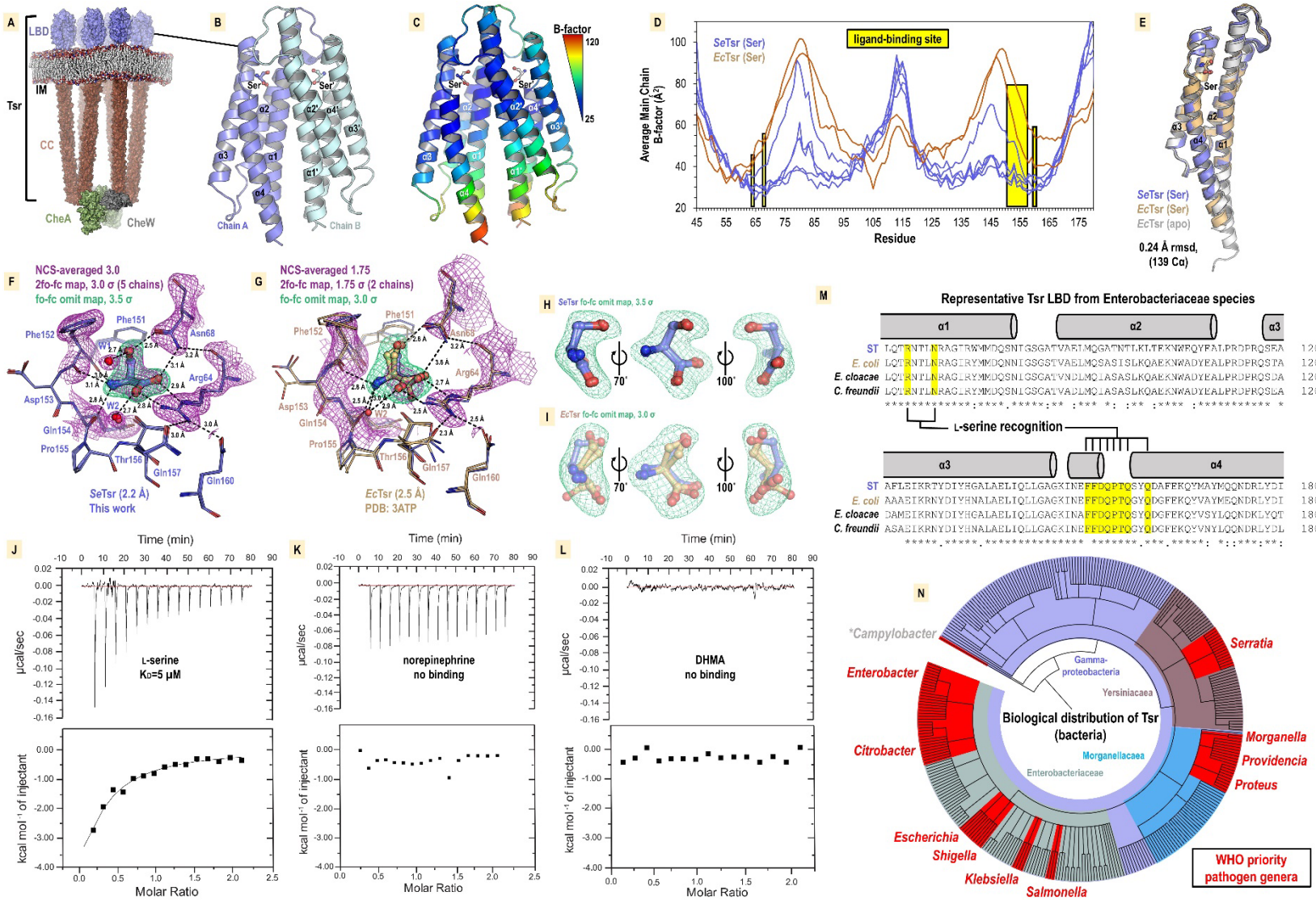
A
LBD
IM
Tsr
CC
CheA
CheW
B
Chain A
Chain B
C
B-factor
120
25
D
ligand-binding site
SeTsr (Ser)
EcTsr (Ser)
Average Main Chain B-factor (Å²)
Residue
E
SeTsr (Ser)
EcTsr (Ser)
EcTsr (apo)
0.24 Å rmsd, (139 Cα)
F
NCS-averaged 3.0
2fo-fc map, 3.0 σ (5 chains)
fo-fc omit map, 3.5 σ
SeTsr (2.2 Å)
This work
G
NCS-averaged 1.75
2fo-fc map, 1.75 σ (2 chains)
fo-fc omit map, 3.0 σ
EcTsr (2.5 Å)
PDB: 3ATP
H
SeTsr fo-fc omit map, 3.5 σ
I
EcTsr fo-fc omit map, 3.0 σ
M
Representative Tsr LBD from Enterobacteriaceae species
L-serine recognition
N
Biological distribution of Tsr (bacteria)
Campylobacter
Enterobacter
Citrobacter
Escherichia
Shigella
Klebsiella
Salmonella
Serratia
Morganella
Providencia
Proteus
Gamma-proteobacteria
Yersiniacaea
Morganellacaea
Enterobacteriaceae
WHO priority pathogen genera
J
L-serine
KD=5 μM
K
norepinephrine
no binding
L
DHMA
no binding
Time (min)
μcal/sec
kcal mol⁻¹ of injectant
Molar Ratio

Fig. 5. Structural mechanism underlying L-serine chemosensing. A. Model of the core chemoreceptor signaling unit showing two full-length Tsr chemoreceptor trimer-of-dimers; coiled-coil region (CC), inner membrane (IM) [45]. B. Crystal structure of *S. enterica* Tsr LBD dimer in complex with L-serine (2.2 Å). C-D. Relative order of the *Se*Tsr dimer as indicated by B-factor ($Å^2$). E. Overlay of chains from serine-bound *Se*Tsr (blue), serine-bound *Ec*Tsr (orange), and apo *Ec*Tsr (white). F. Binding of the L-serine ligand as seen with an overlay of the 5 unique chains of the asymmetric unit (AU) in the *Se*Tsr structure. Purple mesh represents non-crystallographic symmetry $2f_o$-f_c omit map electron density (ligand not included in the density calculations). Green mesh represents f_o-f_c omit map difference density for Chain A. Hydrogen bonds to the ligand are shown as dashed black lines with distances indicated in Angstroms (Å). G. The ligand-binding site of serine-bound *Ec*Tsr is shown as in F, with omit map f_o-f_c electron density. The two chains of *Ec*Tsr in the AU are overlaid (orange) with one chain of serine-bound *Se*Tsr (blue). H-I. Closeup view of the L-serine ligand and f_o-f_c omit map density for the *Se*Tsr (blue) and *Ec*Tsr (orange) structures, respectively. J-L. Isothermal titration calorimetry analyses of the *Se*Tsr LBD with L-serine, NE, or DHMA. M. Sequence conservation among Enterobacteriaceae with residues of the L-serine ligand-binding pocket highlighted. N. Biological distribution of Tsr homologues. See also Move S7, Data S1, and Table S2.
(gray, n=16). Data are means and error is SEM. See also Fig. S2, Fig. S3, Fig. S4, Movie S4, Movie S5, Movie S6.

The crystal structure of *Se*Tsr LBD contains five monomers in the asymmetric unit, providing five independent views of the L-serine binding site, with homodimers formed between Chains A and B, C and D, and E and its crystal symmetry mate, E′ (Fig. 5B). Lower B-factors in the *Se*Tsr ligand binding region are indicative of greater order, reflecting that our structure is fully serine-bound (Fig. 5C-D). *Se*Tsr and *Ec*Tsr possess high sequence similarity in the LBD region (82.1% identity), and as expected, retain a similar global structure with all chains of serine-bound *Se*Tsr (5), serine-bound *Ec*Tsr (2), and apo *Ec*Tsr (2) overlaying within 0.24 Å rmsd over 139 C_α (Fig. 5E).

Molecular recognition of L-serine by SeTsr

The higher resolution (+0.3 Å) of the *Se*Tsr structure, and full occupancy of the ligand, provide a much-improved view of the interactions that facilitate specific recognition of L-serine (Fig. 5F-G). Using non-crystallographic symmetry averaging, we leveraged the five independent *Se*Tsr monomers to generate a well-defined $2f_o$-f_c map of the L-serine ligand and residues involved in ligand coordination (Fig. 5F, Movie S7). Omit-map difference density, which is calculated in the absence of a modeled ligand and reduces potential bias in the electron density map, was fit well by the placement of the L-serine ligand (Fig. 5F). In this orientation, the ligand is in an optimal energetic conformation that satisfies all possible hydrogen bonding interactions: the positively-

charged peptide amine donates hydrogen bonds to the backbone carbonyl oxygens of Phe151, Phe152, and Gln154, the negatively-charged ligand carboxyl group donates hydrogen bonds to the Arg64 guanidinium group, the Asn68 side change amine, and a water (W2), and the ligand hydroxyl sidechain donates a hydrogen bond to the Asn68 sidechain oxygen, and accepts a hydrogen bond from a water (W1) (Fig. 5F, Movie S7). All five chains of the *Se*Tsr structure are consistent in the positions of the ligand and surrounding residues (Fig. 5F, Movie S7).

With the aid of the improved view provided by our *Se*Tsr structure, we noticed the L-serine to be positioned differently than modeled into the weak density of the *Ec*Tsr structure (Fig. 5F-G, Movie S7). The *Ec*Tsr structure has the serine positioned with the sidechain hydroxyl facing into the pocket toward Asn68, and the orientations of Asn68, Phe152, Asp153, and Gln157 ligand binding pocket are modeled inconsistently between the two *Ec*Tsr chains in the asymmetric unit (Fig. 5G). Calculating f_o-f_c omit map density for both structures shows clear support for our new *Se*Tsr ligand orientation, and an overlay with the *Ec*Tsr f_o-f_c omit map data indicates this orientation would also fit well the electron density for that structure (Fig. 5H-I). Thus, the data in both *S. enterica* and *E. coli* Tsr structures support a revised orientation of the ligand in which the L-serine side chain hydroxyl faces outward from the pocket and toward the solvent.

SeTsr LBD binds L-serine, but not NE or DHMA.

Despite a lack of chemotactic responses to NE and DHMA in our CIRA experiments (Fig. S2, Movie S5-6), our uncertainty lingered as to whether these neurotransmitters are sensed through Tsr. Prior work created theoretical models of NE and DHMA binding *Ec*Tsr at the L-serine site, and proposed this as the molecular mechanism underlying *E. coli* chemoattraction to these compounds [42]. However, with our new experimentally-determined *Se*Tsr LBD crystal structure in hand, it is clear that the hydrogen bonding network is specific for L-serine (Fig. 5F, Movie S7), and we were doubtful such dissimilar ligands as NE or DHMA would be accommodated. We note that the amino acids that constitute the L-serine binding pocket are identical between *Se*Tsr and *Ec*Tsr (Fig. 5F-G), and so at the protein level *Se*Tsr LBD and *Ec*Tsr LBD should have similar molecular functions and ligand specificity.

Despite several studies reporting a direct role of Tsr in directing chemoattractant responses to NE and DHMA, no direct evidence of ligand-binding has ever been presented.

Thus, we performed isothermal titration calorimetry (ITC) experiments, a gold-standard for measuring protein-ligand interactions, to study ligand recognition by *Se*Tsr LBD (Fig. 5J-L). As expected, L-serine produced a robust exothermic binding curve, exhibiting a K_D of approximately 5 µM (Fig. 5J). This matches well with our observation of *S. enterica* chemoattraction requiring a source of L-serine at least 0.5-5 µM (Fig. 4D-E) and with prior ITC data with *Ec*Tsr LBD, which also reported a 5 µM K_D [46]. By comparison, neither NE nor DHMA showed any evidence of binding to *Se*Tsr LBD (Fig. 5K-L). These data confirm *Se*Tsr is a receptor for L-serine, and not NE or DHMA, and further support the mechanism of Tsr-mediated serum chemoattraction to be through L-serine.

Bacteria with tsr genes perform serum chemoattraction

The biological distribution of Tsr chemoreceptors has not been previously characterized. We hypothesized that chemoattraction to serum, mediated through Tsr, might extend beyond *Salmonella* to other bacterial species. We applied our structural insights to define a motif consisting of the amino acids involved in L-serine recognition, and when we analyzed the genomes of Enterobacteriaceae genera such as *Escherichia*, *Citrobacter*, and *Enterobacter*, found that they too possess Tsr-like chemoreceptor genes (Fig. 5M). We next conducted a comprehensive search for chemoreceptor genes containing the L-serine recognition motif, resulting in the creation of a database containing all organisms that possess putative Tsr orthologues (Fig. 5N, Data S1). The biological distribution of Tsr reveals the chemoreceptor to be widely conserved among Gammaproteobacteria, particularly within the families Enterobacteriaceae, Morganelliaceae, and Yersiniaceae (Fig. 5N). We identified that many WHO priority pathogens are among the species that have Tsr, leading us to suspect these pathogens and pathobionts also perform serum chemoattraction. To address this question, we performed CIRA analyses with human serum and the bacterial strains *E. coli* MG1655 and *C. koseri* BAA-895, the latter being a clinical isolate with previously uncharacterized chemotactic behavior. We find that both these strains exhibit chemoattraction to human serum on time scales and magnitudes similar to experiments with *Salmonella* (Fig. 6A-C). Based on these results, we infer serum chemoattraction to be a phenomenon common among Enterobacteriaceae species, and may also occur in Gammaproteobacteria priority pathogen genera such as *Serratia*, *Providencia*, *Morganella*, and *Proteus* (Fig. 5N).

Fig. 6. Enterobacteriaceae possessing Tsr display chemoattraction to human serum. A-C. Response of *C. koseri* BAA-895 (n=3, 37° C) and *E. coli* MG1655 to human serum (n=3, 30° C), shown as max projections. Plotted data shown are means averaged over 1 s, and error is SEM. See also Movie S8, Movie S9, and Table S1.

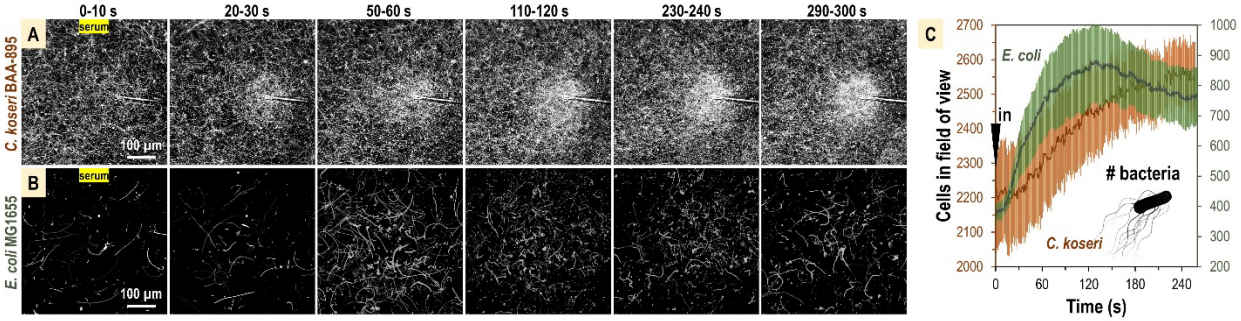

Discussion

The most common outcome for gastrointestinal bacterial infections is that they are resolved by the immune system without chronic infection or lingering pathologies (Fig. 1). To understand why, in rare circumstances, infections do persist, become chronic, systemic, and life-threatening, we must uncover the mechanisms at the crossroads where pathogens divert from the routine course of infection and do something unusual. An emerging area of interest in the axis of gut-microbe health, is how the behavior of gut microbes can shift in response to inflammation, antibiotic usage, and pathogen invasion, into a state of dysbiosis recalcitrant to treatment [16,48–50]. We can learn about the factors that stimulate microbial-induced pathologies by studying how bacteria respond to host-derived stimuli that are unique to the diseased gut [50]. Here, we have investigated how bacterial chemosensing functions to respond to a source of serum, a chemical feature enteric bacteria only encounter in the event of GI bleeding.

We demonstrated that human serum is a potent chemoattractant, and nutrient source, for Enterobacteriaceae bacteria known for instigating enteric bleeding during infection, and that are

causal agents of bacteriemia and sepsis (Fig. 2-3, Fig. 5-6). Pathologies that compromise the integrity of the GI tract, such as intestinal intra-abdominal abscesses, microperforations, and fistulas associated with IBD, predispose patients to GI bleeding and bacteremia [51,52]. In a broader context, the rapid chemoattractive behavior of Enterobacteriaceae to serum fits into an emerging picture of how host-emitted factors in the diseased gut can drive bacterial tropism for sites of inflammation and injury (Fig. 1) [3,24,53–57]. This behavior is responsible for accumulation of bacteria at lesions, which exacerbates tissue damage, delays wound healing, and increases risk of systemic infection [56,58]. Given the above lines of evidence, bacterial serum chemoattraction could be a risk factor for developing systemic infections.

New contexts for L-serine chemoattraction

We show here that the bacterial chemoattraction response to human serum is robust and rapid; the motile population restructures within 1-2 minutes of serum exposure and the cells increase in density to the point of saturation at the serum source (Fig. 2, Fig. 6). We expect that serum chemoattraction occurs through the cooperative action of multiple bacterial chemoreceptors that perceive several chemoattractant stimuli, but a primary driver of this phenomenon appears to be the chemoreceptor Tsr through recognition of L-serine (Fig. 3). While Tsr is known as a bacterial sensor of L-serine [3,45,59], the physiological sources of L-serine in the gut sensed by Tsr have not been well-defined. One major source is clearly dietary; however new research has raised the possibility that L-serine from damaged tissue may play an important role in diseased gut environments to drive opportunistic pathogenesis. In a recent study using a dextran sodium sulfate (DSS)-colitis model to investigate L-serine utilization by Enterobacteriaceae, L-serine was identified as a critical nutrient that provides metabolic and growth advantages in the inflamed gut [50]. Further, colitis was found to stimulate large increases in the luminal availability of most amino acids and average serine content nearly doubled [50]. A characteristic feature of the DSS-colitis model is fecal bleeding [60], and so the enrichment of amino acids as a result of DSS treatment, including serine, may be attributable to leakage of host metabolites from serum. That pathogenic Enterobacteriaceae are poised to leverage growth advantages from L-serine during colitis may relate to their highly sensitive and rapid chemoattraction to this effector emitted from human serum.

Our structural and molecular studies of the *Salmonell*a Tsr LBD confirm that this chemoreceptor is aptly named and that the ligand-binding site is highly optimized, and selective, for recognition of L-serine (Fig. 4-5). Although the host-derived metabolites NE and DHMA have been reported to be chemoattractants sensed through Tsr, we were unable to reproduce these results in chemotaxis experiments nor binding assays with the purified recombinant protein (Fig. S2, Fig. 5K-L). Our inability to substantiate a structure-function relationship for NE/DHMA signaling indicates these neurotransmitters are not ligands of Tsr. In contrast, L-serine drove chemoattractant responses to a source as low as 500 nM, a binding K_D of 5 µM was established through ITC, and was captured in complex in the *Se*Tsr LBD crystal structure with clearly-defined electron density (Fig. 4, Fig. 5). Interestingly, the well-resolved ligand binding site in this new structure shows the L-serine position was misinterpreted in prior studies, which may necessitate some revisions in understanding how ligand occupancy stimulates signal transduction to CheA and across the chemoreceptor nanoarray (Fig. 5). This structure was also helpful in accurately defining the residues central to L-serine recognition, allowing us to mine genomic databases and report the first extensive characterization of which bacterial species possess Tsr orthologues (Fig. 5). From this database of Tsr sequences we were able to visualize the distribution of Tsr orthologues across biology, which strikingly are enriched among Enterobacteriaceae, but are also present in several other families that include WHO priority pathogens (Fig. 5N, Data S1). This analyses confirms that the bacterial species most commonly associated with bacteremia in patients with IBD possess the Tsr chemoreceptor (Fig. 5 N, Data S1) [26].

In the context of *Salmonella* pathogenesis, it is interesting to note that diverse serovars, which vary in terms of host specificity and epidemiology, exhibit serum chemoattraction and have the ability to utilize serum as a nutrient (Fig. 2H-J, Fig. 4H-K). The specific nutrients responsible for the growth benefits derived from serum remain undefined, however one potential candidate is the presence of energy-rich glycoconjugates, which were previously implicated as nutrients in the inflamed intestine based on the upregulation of galactose utilization operons and the prevalence of lectin-positive stained tissue [61]. Enteric Peyer's patches are primary invasion sites for non-typhoidal *Salmonella*, and these structures are situated close to vasculature that can be damaged through the pathogen's destruction of microfold (M) cells, causing localized bleeding [62]. *S. enterica* Typhimurium uses the chemoreceptor Tsr to locate and invade Peyer's

patches [32], which could involve L-serine chemoattraction originating from serum or necrotic cells. Although GI bleeding is relatively uncommon in *Salmonella* infections overall, it afflicts 60% of infected children under the age of five [63]. Therefore, while we acknowledge that serum chemoattraction is unlikely to be involved in the routine pathogenesis strategy of *Salmonella*, the significant number of bacterial-induced GI bleeding cases, and the association between GI bleeding and bacterial invasion into the bloodstream, provide opportunities for serum chemoattraction to be involved in infection outcomes (Fig. 1) [25,52,64].

Materials and Methods

RESOURCE AVAILABILITY

Lead contact

Further information and requests for resources and reagents should be directed to and will be fulfilled by the lead contact, Arden Baylink (arden.baylink@wsu.edu).

Materials availability

Strains and plasmids generated in this study will be made available upon request by the Lead Contact with a completed Materials Transfer Agreement.

Data availability

The crystal structure of L-serine-bound *Se*Tsr LBD has been deposited to the protein databank as PDB: 8FYV. Any additional information required to reanalyze the data reported in this paper is available from the Lead Contact upon request.

EXPERIMENTAL MODEL AND SUBJECT DETAILS

Bacterial strains

Strains of *S. enterica*, *E. coli*, and *C. koseri* used in this study are described in the Table S1. To generate fluorescent strains, electrically-competent bacterial cultures were prepared through successive washing of cells with ice-cold 10 % glycerol, and then transformed by electroporation (Biorad GenePulser Xcell) with pxS vectors containing either sfGFP, or mPlum, and AmpR

genes [65]. Transformants were isolated through growth on selective media and stored as glycerol stocks for subsequent use. To prepare motile bacterial cells for chemotaxis experiments, bacterial cultures were grown shaking overnight in 2-5 ml tryptone broth (TB) and 50 µg/ml ampicillin (TB+Amp) at 30˚ C or 37˚ C, as needed. The following day, 25 µl of overnight culture was used to inoculated 25 ml of fresh TB+Amp and grown shaking for 3-5 hours to reach optical density 600 (OD_{600}) of approximately 0.5. To better isolate responses to effectors of interest and remove confounding variables, such as pH variation and quorum-signaling molecules, we washed and exchanged the cells into a buffer of defined composition. Bacterial cultures were centrifuged at 1,500 g for 20 minutes and exchanged into a chemotaxis buffer (CB) containing 10 mM potassium phosphate (pH 7), 10 mM sodium lactate, and 100 µM EDTA. Cultures were diluted to approximately OD_{600} 0.2 and allowed to recover rocking gently for 30-60 minutes to become fully motile.

For *in vitro* growth analyses, *S. enterica* strains were grown in Luria-Bertani (LB) media shaking overnight at 37˚ C. The following day, cultures were pelleted by centrifugation and resuspended in a minimal media (MM) containing 47 mM Na_2HPO_4, 22 mM KH_2PO_4, 8 mM NaCl, 2mM $MgSO_4$, 0.4% glucose (w/v) 11.35 mM $(NH_4)_2SO_4$, 100 µM $CaCl_2$. 5 µl of the overnight cultures at 0.05 A_{600} were used to inoculate fresh solutions of 200 µl of MM, or additives diluted into MM (human serum or L-serine), in a 96-well microtiter plate. A plate reader was used to monitor cell growth while shaking at 37˚ via A_{600} readings every 5 minutes.

METHOD DETAILS

Chemosensory injection rig assay (CIRA)

Our CIRA system is based on prior work, with several notable changes to methodology, as described. [5,6,66]. The CIRA apparatus was constructed using a pump for injection (either a refurbished Eppendorf Transjector 5246 or Femtojet 4i) and universal capillary holder, with solutions injected through Femtotip II glass microcapillaries (Eppendorf), and the microcapillary position controlled with a MP-285 micromanipulator (Sutter) at a 30˚ angle of attack. To generate a microgradient, a constant flow from the microcapillary was induced by applying compensation pressure (P_c) of 35 hPa. The stability of the microgradient under these conditions was determined with Alexa488 dye (ThermoFisher), and the flow was determined empirically

with methylene blue dye to be approximately 300 femtoliters per minute at 30˚ C (Fig. S1). Pooled off-the-clot human serum was obtained from Innovative Research; serum was deidentified and had no additional chemical additives and is presumed to be fully active. Treatment solutions were filtered through a 0.2 µm filter and injected as-is (serum) or diluted in CB (serine, aspartate, NE, DHMA). Serine racemase treatment of serum was performed with the addition of 5 µl of proprietary serine racemase solution from a DL-serine assay kit (Abcam) to 1 ml of serum for 3 h. For each CIRA experiment, a fresh pond of 50 µl of motile bacteria was mounted open to air on a 10-well slide (MP Biomedicals), and the microcapillary containing the treatment of interest was lowered into the pond. Bacterial responses were imaged with an inverted Nikon Ti2 Eclipse microscope with an enclosed heated sample chamber. Temperature of experiments were at 37 ˚C, unless otherwise indicated.

CIRA microgradient modeling

Diffusion is modeled as a 3D process in which the diffusive species is slowly and continuously introduced at a fixed point in a large ambient fluid volume. The species to be injected is prepared at concentration M_s (typically in the range of 0.5 µM-5 mM) and is injected at a volume rate Q = 305.5 fl/min. The species diffuses into the ambient fluid with diffusion constant D. The governing equation for the diffusion of a species introduced continuously at a point source is:

$$C(r,t) = \frac{q}{4\pi D r} erfc \frac{r}{2\sqrt{Dt}}$$

where r is the distance from the point source, t is the time from injection initiation, and $q = M_s Q$ is the injection rate of the species, and C is the species concentration. We can simplify the presentation by defining a characteristic length scale r_0, characteristic time t_0, and dimensionless variables as:

$$r_0 = \frac{Q}{4\pi D}, t_0 = \frac{Q^2}{(8\pi)^2 D^3}, \bar{r} = \frac{r}{r_0}, \bar{t} = \frac{t}{t_0}.$$

Then, we have the diffusion-driven concentration model:

$$C(\bar{r},\bar{t}) = \frac{M_s}{\bar{r}} erfc \frac{\bar{r}}{\sqrt{\bar{t}}}$$

Representative diffusion coefficients are: A488, $4.00 \times 10^{-6}\,\mathrm{cm}^2/\mathrm{s}$; L-serine, $8.71 \times 10^{-6}\,\mathrm{cm}^2/\mathrm{s}$; L-aspartate, $9.35 \times 10^{-6}\,\mathrm{cm}^2/\mathrm{s}$. Due to the small injection rate, our assumption of a point source leads to a model that is valid at distances $r \gg r_0 \sim 1$ nm and times $t \gg t_0 \sim 1$ ns. We also consider the total species quantity integrated along a viewing direction. The result is:

$$I(\bar{r},\bar{t}) = 2M_s r_0 \int_0^\infty \frac{d\bar{z}}{\sqrt{\bar{z}^2+\bar{r}^2}} erfc \frac{\sqrt{\bar{z}^2+\bar{r}^2}}{\bar{t}}$$

where $\bar{z}$ is the unitless integration variable along the viewing direction. This integral was evaluated numerically by considering the sequence of points $z_k = \frac{k+1}{2}\Delta\bar{z}$ for $k = 1,2,3,\ldots$ and $\Delta\bar{z}$ some small interval. Then, we have the discrete integral approximation:

$$I(\bar{r},\bar{z}) \approx 2M_s r_0 \Delta\bar{z} \sum_{k=1}^{N} (z_k^2+\bar{r}^2)^{-1/2} erfc \frac{\sqrt{z_k^2+\bar{r}^2}}{\bar{t}}.$$

Computations for this work used 1 µm steps extending out to $r = 500$ µm. That is, $\Delta\bar{z} = 1\ \mu\mathrm{m}/r_0$ and $N = 500$.

Cloning and recombinant protein expression

Cloning of the *S. enterica* Tsr LBD construct for recombinant protein expression was performed as a service by Genscript Biotech Corp. The sequence of the periplasmic portion of the ligand-binding domain of *S. enterica* Typhimurium Tsr (gene *STM4533*), corresponding to residues 32-187 of the full-length protein, was encoded into a pet-30a(+) vector (Tsr-LBD-pet-30a(+)), at the NdeI and HindIII sites, with a short N-terminal TEV cleavage tag (MENLYFQ) such that the final expressed protein sequence was:

MENLYFQSLKNDKENFTVLQTIRQQQSALNATWVELLQTRNTLNRAGIRWMMDQSNIG
SGATVAELMQGATNTLKLTEKNWEQYEALPRDPRQSEAAFLEIKRTYDIYHGALAELIQ
LLGAGKINEFFDQPTQSYQDAFEKQYMAYMQQNDRLYDIAVEDNNS

Chemically-competent Rosetta BL21(DE3) *E. coli* (Millipore Sigma) were transformed by heat shock with the Tsr-LBD-pet-30a(+) vector, and transformants identified by growth on selective media containing 20 µg/ml (LB+Kan). Cells were grown overnight in 5 ml LB+Kan. The following day, 1 ml of overnight culture was used to inoculate 1 L of fresh LB+Kan, and cultures were grown to OD_{600} 0.6-0.8 and induced with 0.4 mM isopropyl β-D-1-thiogalactopyranoside (IPTG). After growth for 3 H at 37˚ C cells, were harvested by centrifugation.

Purification of recombinant SeTsr LBD

The cell pellet was resuspended in a lysis buffer containing 50 mM Tris pH 7.5, 0.1 mM DTT, 1 mM EDTA, 5 mg DNAse I, and 1 cOmplete protease inhibitor tablet per 1 L of culture (Sigma Aldrich), and cells were lysed by sonication. After, the lysate was kept on ice and adjusted to 20 % ammonium sulfate saturation and stirred at 4˚ C for 30 minutes. Lysate was centrifuged at 15,000 rpm for 30 minutes in a Beckman ultracentrifuge. The soluble fraction was retained, and an ammonium precipitation trial was conducted; the 20-40% fraction contained the majority of the Tsr LBD protein and was used for subsequent purification. The protein solution was dialyzed for 16 hours against 4 L of 20 mM Tris, pH 7.5, 20 mM NaCl, and 0.1 mM EDTA, then run over an anion exchange column and FPLC (Akta). The purest fractions were pooled and treated with 0.3 mg/ml TEV protease, and the protein solution was dialyzed against 4 L of 50 mM Tris pH 8, 0.5 mM EDTA, and 1 mM EDTA for 48 h at 4˚ C. Subsequently, the cleaved protein solution was exchanged into a buffer of 50 mM Tris pH 7.5, 1 mM EDTA, and 150mM NaCl, and purified by gel filtration with an S200 column and FPLC. Pure protein fractions were pooled, concentrated to 7 mg/ml, and flash frozen in liquid N_2.

Protein crystallography

Initial crystallization trials of *Se*Tsr LBD were performed with either TEV-cleaved or uncleaved protein samples at 7 mg/ml with +/- 2 mM L-serine and using 96-well matrix screens set up with a Mosquito robot (SPT Labtech). We only observed crystal hits with the cleaved, serine-treated

crystals, the best of which was 0.056 M sodium phosphate, 1.344 M potassium phosphate, pH 8.2. This condition was further optimized to be 1.5 µl *Se*Tsr LBD protein (7 mg/ml), 0.5 µl of 8 mM L-serine, and 1.5 µl 1.69 M potassium phosphate pH 9.7, grown via hanging drop vapor diffusion with a 1 ml reservoir of 1.69 M potassium phosphate pH 9.7 at 22˚ C. Attempts at using cryoprotectants were unsuccessful and resulted in crystals dissolving or diminished diffraction, so crystals were scooped directly from drops and flash frozen in liquid N_2. X-ray diffraction data were collected at the Berkeley Advanced Light Source (ALS) beamline 5.0.3. Out of approximately 100 crystals examined, only one diffracted to high resolution and was not impacted by crystal twinning.

Data were indexed with DIALS [67], scaled with Aimless [68], and found to correspond well to space group $C2_1$. A conservative final resolution cutoff of 2.2 Å was applied on the basis of $CC_{1/2}$ >0.3 and completeness >50% in the highest resolution shell [69].

The serine-bound *Ec*Tsr structure (PDB: 3atp) was utilized as a molecular replacement search model with Phaser-MR in Phenix [70] to solve the *Se*Tsr LBD dataset with five monomers in the asymmetric unit. 10% of the data were designated as R_{free} flags and the initial model was adjusted by setting all B-factors to 30 $Å^2$ and coordinates were randomized by 0.05 Å to reduce bias from the starting model. Subsequent model building with Coot [71] and refinement with Phenix enabled placement of residues 42-182 and the serine ligand. However, residues 32-41 and 183-187 could not be resolved and were not modeled, causing the R/R_{free} values to being slightly elevated for a model of this resolution. Riding hydrogen atoms and translation, libration, screw refinement was applied and contributed to reduced R factors. The strongest remaining difference peak is along a symmetry axis. The final model R/R_{free} values were 24.1/25.8 %, with a 99th percentile all-atom MolProbity clashscore, and a 100th percentile overall MolProbity score [72]. Crystallographic statistics are listed in Table S2. The structure was deposited to the protein data bank as entry 8FYV.

Isothermal titration calorimetry ligand binding studies (ITC)

ITC experiments were performed in 50 mM Tris, 150 mM NaCl, 1 mM EDTA, pH 7.5, at 25 °C. We dialyzed the protein into the experimental buffer and dissolved the small molecule ligands into the same buffer. Protein concentrations were ~50 µM; titrant concentrations were 500 µM. Samples were degassed prior to experiments. All experiments were performed on a MicroCal

ITC-200 system (GE Healthcare), with the gain set to "low" and a syringe stir speed of 750 rpm. Titration data for the serine experiments were fit to a single-site binding model using the built-in ITC analysis software.

Mass Spectrometry

Determination of molar content of total serine in human serum samples was performed as a service through the University of Washington Mass Spectrometry Center. Samples were analyzed on the Waters TQ #1 instrument using a Thermo Hypersil Gold PFP column (2.1 x 100) with 0.1% heptafluorobutyric acid (HFBA) in water and acetonitrile.

QUANTIFICATION AND STATISTICAL ANALYSIS

Quantification of CIRA data

To determine relative numbers of cells over time, a ratio of fluorescence intensity per cell was calculated using ImageJ. Fluorescence intensity was used as a readout of relative cell count over time using the 'plot profile' function in ImageJ [73]. Cell numbers were normalized to a baseline of "100 %" at the start of treatment (shown as time 0). Distribution of the bacterial population was quantified through use of the 'radial profile' ImageJ plugin. Radial distribution data were normalized by setting the field of view periphery as the baseline of "1-fold," which we defined as 240 µm distance from the source. Images and videos shown were processed using the 'enhance contrast' function in ImageJ and adjusting intensity thresholds to normalize fluorescence intensity per cell across channels. For experiments with non-fluorescent cells, equivalent procedures were performed using phase contrast data and enumeration of cells over time using a Matlab-based tracking software [6].

Statistical Analyses

Data from replicate experiments were averaged and interpreted on the basis of their mean, standard error of the mean, and effect sizes. Effect sizes for data are indicated as Cohen's *d* value:

$$\mathrm{d} = \frac{\mathrm{M}_1 - \mathrm{M}_2}{\sigma_{\mathrm{pooled}}}$$

where:

$$\sigma_{pooled} = \sqrt{\frac{{\sigma_1}^2 + {\sigma_2}^2}{2}}$$

Where relevant, *p*-values were calculated using either one-sided or unpaired two-sided tests, with significance determined at $p<0.05$:

$$t = \frac{\bar{\mathrm{x}}_1 - \bar{\mathrm{x}}_2}{\sqrt{s^2\left(\frac{1}{n_1} + \frac{1}{n_2}\right)}}$$

where:

$$s^2 = \frac{\sum_{i=1}^{n_1}(x_i - \bar{\mathrm{x}}_1)^2 + \sum_{j=1}^{n_2}(x_j - \bar{\mathrm{x}}_2)^2}{n_1 + n_2 - 2}$$

Acknowledgements

Funding for this work was provided by NIAID under award numbers 1K99AI148587 and 4R00AI148587-03, and startup funding from Washington State University to AB. We thank Karen Guillemin (University of Oregon) for the Eppendorf Transjector used for the CIRA experiments. We thank Nikki Shariat (University of Georgia, Athens), Nkuchia Mikanatha and Pennsylvania NARMS and GenomeTrakr Programs, and Andreas Bäumler (University of California, Davis) for providing the *Salmonella* strains used in this work. Beamline 5.0.3 of the Advanced Light Source, a DOE Office of Science User Facility under Contract No. DE-AC02-05CH11231, is supported in part by the ALS-ENABLE program funded by the National Institutes of Health, National Institute of General Medical Sciences, grant P30 GM124169-01. All research on human samples was performed in accordance with, and approval of, the Institutional Biosafety Committee at Washington State University.

Author Contributions

A.B. and S.G. conducted the CIRA experiments. S.G. and Z.G. performed growth curve analyses with human serum and purified L-serine. A.B., S.G., and Z.G. performed the crystallographic analyses. T.A. performed the microgradient modeling. M.S. and M.J.H. performed the ITC experiments. All authors contributed to data analyses and writing of the manuscript.

Declaration of Interests

A.B. owns Amethyst Antimicrobials, LLC.

References

1. Gumerov, V. M., Andrianova, E. P. & Zhulin, I. B. Diversity of bacterial chemosensory systems. *Current Opinion in Microbiology* **61**, 42–50 (2021).
2. Wadhwa, N. & Berg, H. C. Bacterial motility: machinery and mechanisms. *Nat Rev Microbiol* **20**, 161–173 (2022).
3. Zhou, B., Szymanski, C. M. & Baylink, A. Bacterial chemotaxis in human diseases. *Trends in Microbiology* (2022) doi:10.1016/j.tim.2022.10.007.
4. Huang, J. Y., Sweeney, E. G., Guillemin, K. & Amieva, M. R. Multiple Acid Sensors Control Helicobacter pylori Colonization of the Stomach. *PLOS Pathogens* **13**, e1006118 (2017).
5. Huang, J. Y. *et al.* Chemodetection and Destruction of Host Urea Allows Helicobacter pylori to Locate the Epithelium. *Cell Host Microbe* **18**, 147–156 (2015).
6. Perkins, A., Tudorica, D. A., Amieva, M. R., Remington, S. J. & Guillemin, K. Helicobacter pylori senses bleach (HOCl) as a chemoattractant using a cytosolic chemoreceptor. *PLoS Biol* **17**, e3000395 (2019).
7. Jakuszeit, T., Lindsey-Jones, J., Peaudecerf, F. J. & Croze, O. A. Migration and accumulation of bacteria with chemotaxis and chemokinesis. *Eur Phys J E Soft Matter* **44**, 32 (2021).

8. Kearns, D. B. A field guide to bacterial swarming motility. *Nat Rev Microbiol* **8**, 634–644 (2010).
9. Perkins, A. *et al.* A Bacterial Inflammation Sensor Regulates c-di-GMP Signaling, Adhesion, and Biofilm Formation. *mBio* **12**, e00173-21 (2021).
10. Westerman, T. L., McClelland, M. & Elfenbein, J. R. YeiE Regulates Motility and Gut Colonization in Salmonella enterica Serotype Typhimurium. *mBio* **12**, e03680-20 (2021).
11. Ligthart, K., Belzer, C., de Vos, W. M. & Tytgat, H. L. P. Bridging Bacteria and the Gut: Functional Aspects of Type IV Pili. *Trends in Microbiology* **28**, 340–348 (2020).
12. Murray, C. J. *et al.* Global burden of bacterial antimicrobial resistance in 2019: a systematic analysis. *The Lancet* **399**, 629–655 (2022).
13. Tacconelli, E. *et al.* Discovery, research, and development of new antibiotics: the WHO priority list of antibiotic-resistant bacteria and tuberculosis. *The Lancet Infectious Diseases* **18**, 318–327 (2018).
14. Robinson, C. D. *et al.* Host-emitted amino acid cues regulate bacterial chemokinesis to enhance colonization. *Cell Host & Microbe* **29**, 1221-1234.e8 (2021).
15. Lee, J.-H. & Lee, J. Indole as an intercellular signal in microbial communities. *FEMS Microbiology Reviews* **34**, 426–444 (2010).
16. Belizário, J. E. & Faintuch, J. Microbiome and Gut Dysbiosis. in *Metabolic Interaction in Infection* (eds. Silvestre, R. & Torrado, E.) 459–476 (Springer International Publishing, 2018). doi:10.1007/978-3-319-74932-7_13.
17. Rogers, A. W. L., Tsolis, R. M. & Bäumler, A. J. Salmonella versus the Microbiome. *Microbiology and Molecular Biology Reviews* **85**, e00027-19 (2020).

18. Donaldson, G. P., Lee, S. M. & Mazmanian, S. K. Gut biogeography of the bacterial microbiota. *Nat Rev Microbiol* **14**, 20–32 (2016).
19. Aljarad, Z. & Mobayed, B. B. The mortality rate among patients with acute upper GI bleeding (with/without EGD) at Aleppo University Hospital: A retrospective study. *Ann Med Surg (Lond)* **71**, 102958 (2021).
20. Huang, A. H. *et al.* Survival Impact and Clinical Predictors of Acute Gastrointestinal Bleeding in Patients With Bloodstream Infection. *J Intensive Care Med* **36**, 63–69 (2021).
21. Kim, B. S. M. *et al.* Diagnosis of gastrointestinal bleeding: A practical guide for clinicians. *World J Gastrointest Pathophysiol* **5**, 467–478 (2014).
22. Moledina, S. M. & Komba, E. Risk factors for mortality among patients admitted with upper gastrointestinal bleeding at a tertiary hospital: a prospective cohort study. *BMC Gastroenterology* **17**, 165 (2017).
23. Saltzman, J. R. Approach to acute upper gastrointestinal bleeding in adults. (2022).
24. Scales, B. S. & Huffnagle, G. B. The Microbiome in Wound Repair and Tissue Fibrosis. *J Pathol* **229**, 323–331 (2013).
25. Weber, A., Sauk, J. & Limketkai, B. P130 LEADING CAUSES OF MORTALITY IN INFLAMMATORY BOWEL DISEASE: A NATIONWIDE ANALYSIS. *Gastroenterology* **158**, S41–S42 (2020).
26. Goren, I. *et al.* Risk of bacteremia in hospitalised patients with inflammatory bowel disease: a 9-year cohort study. *United European Gastroenterol J* **8**, 195–203 (2020).
27. Murdoch, C. C. & Skaar, E. P. Nutritional immunity: the battle for nutrient metals at the host–pathogen interface. *Nat Rev Microbiol* **20**, 657–670 (2022).

28. Cheng, Z. *et al.* Glycine, serine and threonine metabolism confounds efficacy of complement-mediated killing. *Nat Commun* **10**, 3325 (2019).
29. Xu, D. & Lu, W. Defensins: A Double-Edged Sword in Host Immunity. *Front Immunol* **11**, 764 (2020).
30. Medicine, C. for V. Get the Facts about Salmonella. *FDA* (2020).
31. Tsolis, R. M. *et al.* Identification of a Putative Salmonella enterica Serotype Typhimurium Host Range Factor with Homology to IpaH and YopM by Signature-Tagged Mutagenesis. *Infection and Immunity* **67**, 6385–6393 (1999).
32. Rivera-Chávez, F. *et al.* Energy Taxis toward Host-Derived Nitrate Supports a Salmonella Pathogenicity Island 1-Independent Mechanism of Invasion. *mBio* **7**, e00960-16 (2016).
33. Winter, S. E. *et al.* Gut inflammation provides a respiratory electron acceptor for Salmonella. *Nature* **467**, 426–429 (2010).
34. Rivera-Chávez, F. *et al.* Salmonella uses energy taxis to benefit from intestinal inflammation. *PLoS Pathog* **9**, e1003267 (2013).
35. Ferrari, R. G. *et al.* Worldwide Epidemiology of Salmonella Serovars in Animal-Based Foods: a Meta-analysis. *Appl Environ Microbiol* **85**, e00591-19 (2019).
36. Matilla, M. A., Velando, F., Martín-Mora, D., Monteagudo-Cascales, E. & Krell, T. A catalogue of signal molecules that interact with sensor kinases, chemoreceptors and transcriptional regulators. *FEMS Microbiology Reviews* **46**, fuab043 (2022).
37. He, Q. *et al.* Serum Serine and the Risk of All-Cause Mortality: A Nested Case-Control Study From the China Stroke Primary Prevention Trial (CSPPT). *Frontiers in Nutrition* **9**, (2022).

38. Miller, D. E., Ferreira, C. R., Scott, A. I. & Chang, I. J. Pharmacokinetics of oral l-serine supplementation in a single patient. *Molecular Genetics and Metabolism Reports* **24**, 100607 (2020).

39. Pitkänen, H. T., Oja, S. S., Kemppainen, K., Seppä, J. M. & Mero, A. A. Serum amino acid concentrations in aging men and women. *Amino Acids* **24**, 413–421 (2003).

40. Kopin, I. J., Lake, R. C. & Ziegler, M. Plasma levels of norepinephrine. *Ann Intern Med* **88**, 671–680 (1978).

41. Steuer, A. E. *et al.* Impact of Cytochrome P450 2D6 Function on the Chiral Blood Plasma Pharmacokinetics of 3,4-Methylenedioxymethamphetamine (MDMA) and Its Phase I and II Metabolites in Humans. *PLOS ONE* **11**, e0150955 (2016).

42. Orr, A. A. *et al*. Molecular Mechanism for Attractant Signaling to DHMA by E. coli Tsr. *Biophysical Journal* **118**, 492–504 (2020).

43. Pasupuleti, S. *et al*. Chemotaxis of Escherichia coli to norepinephrine (NE) requires conversion of NE to 3,4-dihydroxymandelic acid. *J Bacteriol* **196**, 3992–4000 (2014).

44. Hashimoto, K. *et al.* Decreased Serum Levels of D-Serine in Patients With Schizophrenia: Evidence in Support of the N-Methyl-D-Aspartate Receptor Hypofunction Hypothesis of Schizophrenia. *Archives of General Psychiatry* **60**, 572–576 (2003).

45. Cassidy, C. K. *et al.* Structure and dynamics of the E. coli chemotaxis core signaling complex by cryo-electron tomography and molecular simulations. *Commun Biol* **3**, 1–10 (2020).

46. Tajima, H. *et al.* Ligand Specificity Determined by Differentially Arranged Common Ligand-binding Residues in Bacterial Amino Acid Chemoreceptors Tsr and Tar*. *Journal of Biological Chemistry* **286**, 42200–42210 (2011).

47. Burt, A. *et al*. Complete structure of the chemosensory array core signalling unit in an E. coli minicell strain. *Nat Commun* **11**, 743 (2020).

48. Rivera-Chávez, F., Lopez, C. A. & Bäumler, A. J. Oxygen as a driver of gut dysbiosis. *Free Radical Biology and Medicine* **105**, 93–101 (2017).

49. Zeng, M. Y., Inohara, N. & Nuñez, G. Mechanisms of inflammation-driven bacterial dysbiosis in the gut. *Mucosal Immunol* **10**, 18–26 (2017).

50. Kitamoto, S. *et al*. Dietary L-serine confers a competitive fitness advantage to Enterobacteriaceae in the inflamed gut. *Nat Microbiol* **5**, 116–125 (2020).

51. Satoh, K., Okuyama, M., Furuya, T., Irie, Y. & Nakae, H. Severe Sepsis Caused by Bacteria That Entered via the Intestinal Tract: A Case of Crohn's Disease in a Child. *Cureus* **12**, e9822.

52. Vohra, I., Attar, B., Sharma, S., Katiyar, V. & Jaiswal, M. P129 INPATIENT OUTCOMES OF SEPSIS IN INFLAMMATORY BOWEL DISEASE PATIENTS: A 2016 NATIONWIDE INPATIENT SAMPLE ANALYSIS. *Inflammatory Bowel Diseases* **26**, S25–S26 (2020).

53. Aihara, E. *et al*. Motility and Chemotaxis Mediate the Preferential Colonization of Gastric Injury Sites by Helicobacter pylori. *PLOS Pathogens* **10**, e1004275 (2014).

54. Callahan, S. M., Dolislager, C. G. & Johnson, J. G. The Host Cellular Immune Response to Infection by Campylobacter Spp. and Its Role in Disease. *Infect Immun* **89**, e00116-21.

55. Croxen, M. A. & Finlay, B. B. Molecular mechanisms of Escherichia coli pathogenicity. *Nat Rev Microbiol* **8**, 26–38 (2010).

56. Hanyu, H. *et al*. Helicobacter pylori Uses the TlpB Receptor To Sense Sites of Gastric Injury. *Infect Immun* **87**, e00202-19 (2019).

57. Rivera-Chávez, F. *et al.* Salmonella Uses Energy Taxis to Benefit from Intestinal Inflammation. *PLOS Pathogens* **9**, e1003267 (2013).

58. Minasyan, H. Sepsis: mechanisms of bacterial injury to the patient. *Scandinavian Journal of Trauma, Resuscitation and Emergency Medicine* **27**, 19 (2019).

59. Keegstra, J. M., Carrara, F. & Stocker, R. The ecological roles of bacterial chemotaxis. *Nat Rev Microbiol* 1–14 (2022) doi:10.1038/s41579-022-00709-w.

60. Kim, J. J., Shajib, Md. S., Manocha, M. M. & Khan, W. I. Investigating Intestinal Inflammation in DSS-induced Model of IBD. *J Vis Exp* 3678 (2012) doi:10.3791/3678.

61. Stecher, B. *et al.* Motility allows S. Typhimurium to benefit from the mucosal defence. *Cellular Microbiology* **10**, 1166–1180 (2008).

62. Shi, Z. *et al.* Toll-like Receptor 11 (TLR11) Prevents Salmonella Penetration into the Murine Peyer Patches *. *Journal of Biological Chemistry* **287**, 43417–43423 (2012).

63. White, A. E. *et al.* Characteristics of Campylobacter, Salmonella Infections and Acute Gastroenteritis in Older Adults in Australia, Canada, and the United States. *Clin Infect Dis* **69**, 1545–1552 (2019).

64. Irving, P. M., Lusignan, S. de, Tang, D., Nijher, M. & Barrett, K. Risk of common infections in people with inflammatory bowel disease in primary care: a population-based cohort study. *BMJ Open Gastroenterology* **8**, e000573 (2021).

65. Wiles, T. J. *et al.* Modernized Tools for Streamlined Genetic Manipulation and Comparative Study of Wild and Diverse Proteobacterial Lineages. *mBio* **9**, e01877-18 (2018).

66. Howitt, M. R. *et al.* ChePep Controls Helicobacter pylori Infection of the Gastric Glands and Chemotaxis in the Epsilonproteobacteria. *mBio* **2**, e00098-11 (2011).

67. Winter, G. *et al.* DIALS as a toolkit. *Protein Sci* **31**, 232–250 (2022).

68. Winn, M. D. *et al.* Overview of the CCP4 suite and current developments. *Acta Cryst D* **67**, 235–242 (2011).

69. Karplus, P. A. & Diederichs, K. Linking Crystallographic Model and Data Quality. *Science* **336**, 1030–1033 (2012).

70. Adams, P. D. *et al.* PHENIX: a comprehensive Python-based system for macromolecular structure solution. *Acta Cryst D* **66**, 213–221 (2010).

71. Emsley, P. & Cowtan, K. Coot: model-building tools for molecular graphics. *Acta Cryst D* **60**, 2126–2132 (2004).

72. Davis, I. W. *et al.* MolProbity: all-atom contacts and structure validation for proteins and nucleic acids. *Nucleic Acids Res* **35**, W375–W383 (2007).

73. Schneider, C. A., Rasband, W. S. & Eliceiri, K. W. NIH Image to ImageJ: 25 years of image analysis. *Nat Methods* **9**, 671–675 (2012).

74. Beltran, P. *et al.* Reference collection of strains of the Salmonella typhimurium complex from natural populations. *Microbiology* **137**, 601–606 (1991).

75. Shariat, N. *et al.* Subtyping of Salmonella enterica Serovar Newport Outbreak Isolates by CRISPR-MVLST and Determination of the Relationship between CRISPR-MVLST and PFGE Results. *J Clin Microbiol* **51**, 2328–2336 (2013).

76. Shariat, N. *et al.* The combination of CRISPR-MVLST and PFGE provides increased discriminatory power for differentiating human clinical isolates of Salmonella enterica subsp. enterica serovar Enteritidis. *Food Microbiology* **34**, 164–173 (2013).

Supplementary Information

Supplemental Figures

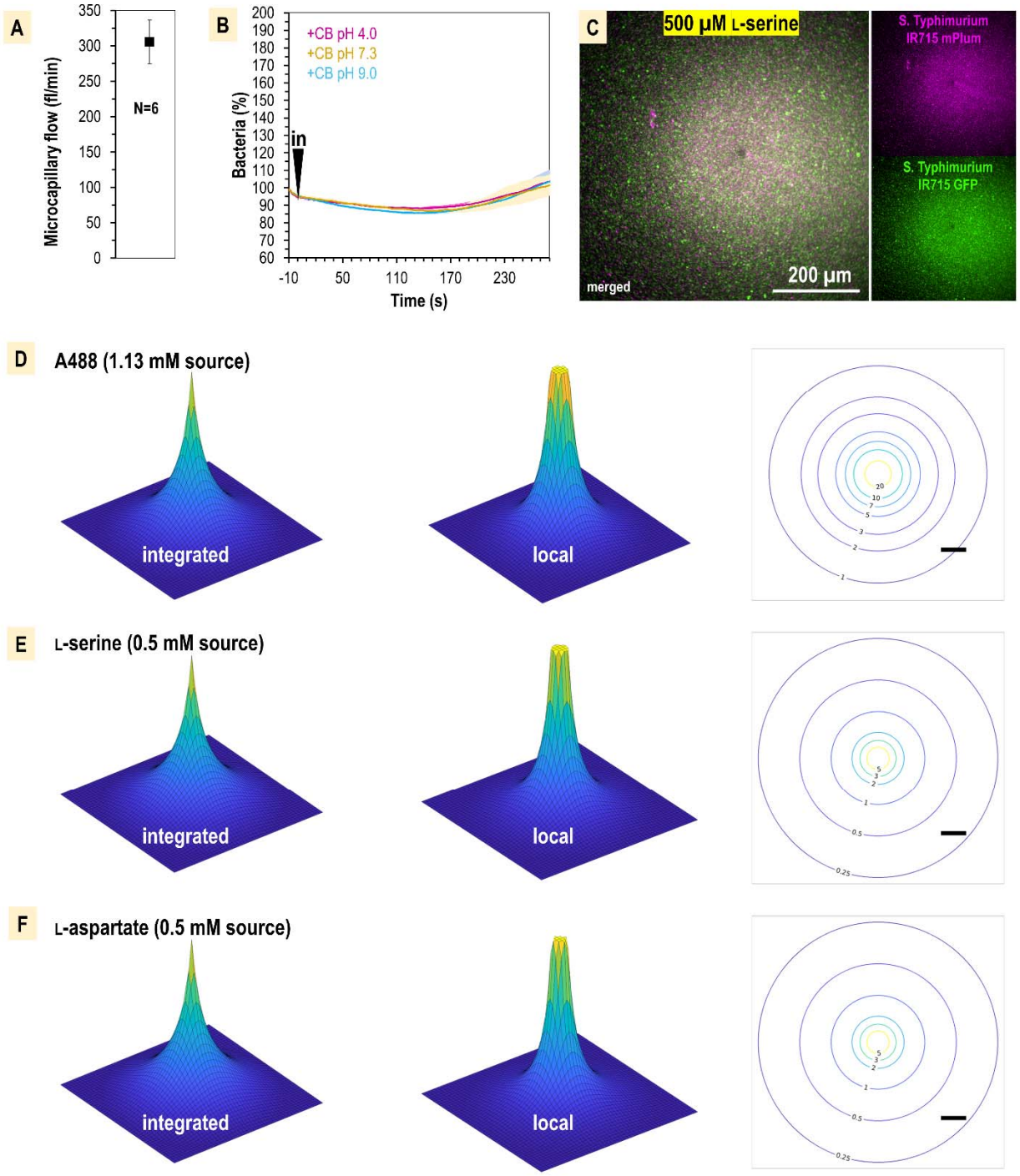

Fig. S1. CIRA experimentation controls and microgradient modeling. A. Average injection flow of treatment solution from the glass microcapillary. Flow was measured through injection of known concentrations of methylene blue dye, diluted in CB, into a 50 µl pond of CB over 20 minutes. After treatments, the absorbance of solutions was measured at 665 nm and quantified based on a standard curve. Applying a compensation pressure of 35 hPa resulted in an average

flow of 305.5 fl/min ± 31. B. CIRA localization in response to treatments of buffered CB of different pH. C. Comparison of responses of GFP versus mPlum strains using CIRA. D-F. Model of the CIRA microgradient for effectors relevant to this study. Topology maps of 1 mm x 1 mm size are shown for each microgradient in an 'integrated' format, which models what is seen by eye from the bottom-up view of the microscopy plane (left), or as the local concentration that would be experienced by a bacterium at a given distance (center). A plane through the center of the treatment sphere is shown (right), with relative concentrations experienced at a given distance expressed in nM units (scale bar is 100 µm).

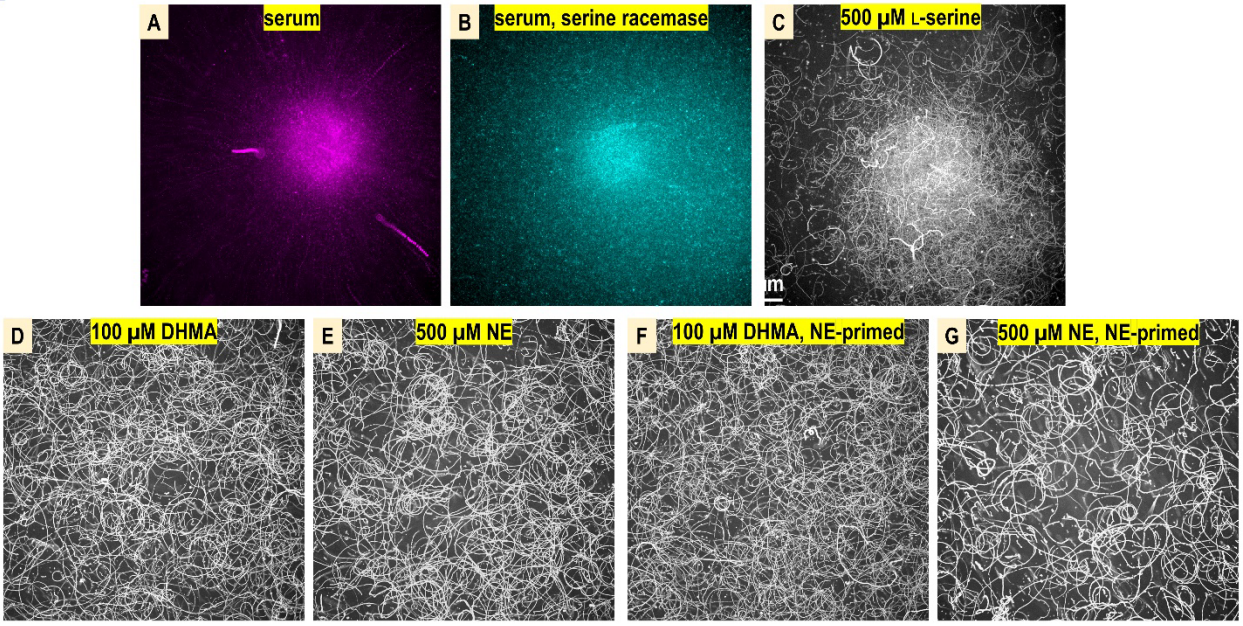

Fig. S2. Comparison of chemotactic responses to serum, serum with serine racemase treatment, L-serine versus DHMA and NE. Shown are max projections from CIRA experiments over a 10 s time period following 300 s of treatments as shown. Experiments F-G utilized cells that were primed with 5 µM NE for 3 hours prior to experimentation.

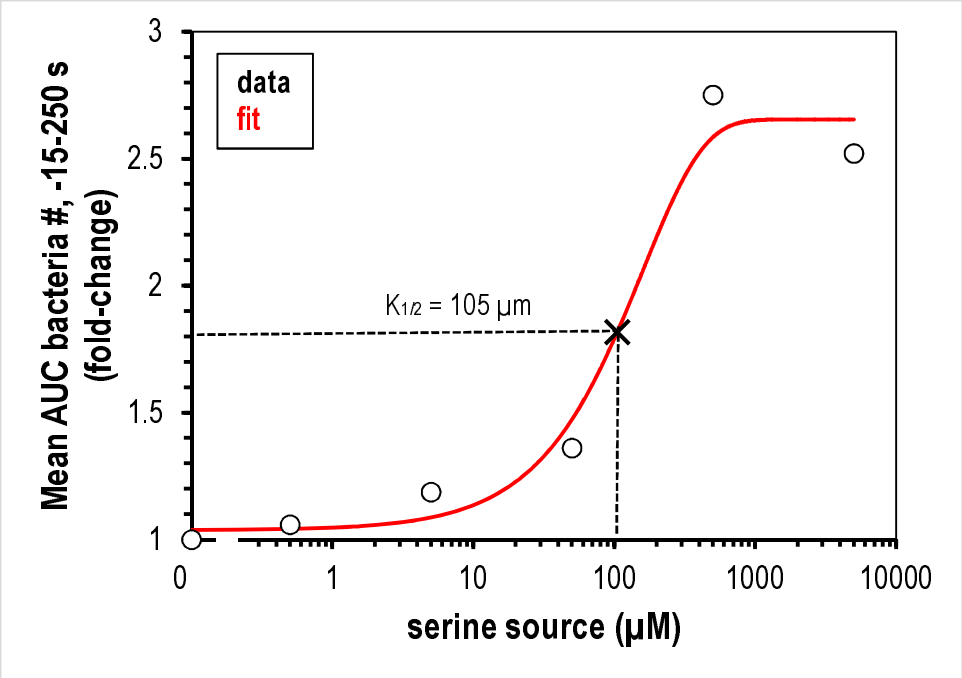

Fig. S3. Calculation of L-serine source required for half-maximal chemoattraction response ($K_{1/2}$). Data are mean AUC values of relative number of bacteria within 150 µm of the treatment location for the -15 s – 250 s range, represented as fold-change. Data are fit with an exponential curve (red line):

$$y = a + be^{-cx}$$

Where a=2.636193, b =-1.616338, and c=0.006282888. $K_{1/2}$ is approximated to be 105 µm (x, dashed lines).

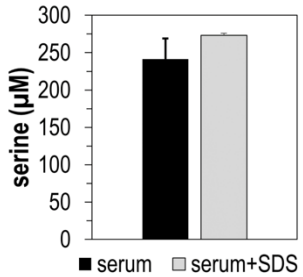

Fig. S4. Total serine present in human serum samples, as determined by mass spectrometry. Treatment with 50 µg recombinant serine dehydratase (SDS) over 4 h did not decrease L-serine content in human serum.

Supplemental Movies

Movie S1. Representative CIRA experiments with Alexa Fluor 488 dye (left) and *S. enterica* Typhimurium IR715 treated with human serum (right). Viewable at: https://www.youtube.com/watch?v=dyrQT2Ni5J8

Movie S2. Representative CIRA experiments comparing responses to human serum between *S. enterica* Typhimurium IR715 (*mplum*) and clinical isolates (*gfp*), as indicated. Viewable at: https://youtu.be/dwtZtoisjrU

Movie S3. Representative CIRA experiments comparing responses to human serum between WT *S. enterica* Typhimurium IR715 (*mplum* in left and center panel) and chemotactic mutants *tsr* (*gfp* in center panel, *mplum* in right panel), and *cheY* (*gfp* in left and right panel). Viewable at: https://youtu.be/O5zsEAqcJw8

Movie S4. Representative CIRA experiments comparing responses to 500 µM L-serine between *S. enterica* Typhimurium IR715 (*mplum*) and clinical isolates (*gfp*), as indicated. Viewable at: https://www.youtube.com/watch?v=p0Tsp06ZHO8

Movie S5. CIRA experiments comparing response of *S.* Typhimurium IR715 to L-serine or to norepinephrine. Cells are unprimed or primed with NE, as indicated. Viewable at: https://youtu.be/pUOlVjKYptc

Movie S6. CIRA experiments showing response of *S.* Typhimurium IR715 to DHMA. Cells are unprimed (left) or primed with NE (right). Viewable at: https://youtu.be/j4YL95QFCuI

Movie S7. Crystal structure of *S. enterica* Typhimurium Tsr LBD and comparison with *E. coli* Tsr LBD crystal structure (pdb: 3ATP). Viewable at: https://youtu.be/OlowDhRLNhA

Movie S8. Representative CIRA experiment showing response of *C. koseri* BAA-895 to human serum. Viewable at: https://youtu.be/9iMJz2OPbso

Movie S9. Representative CIRA experiment showing response of *E. coli* (pxS-gfp) MG1655 to human serum. Viewable at: https://www.youtube.com/watch?v=jq3cj9e52n4

Supplementary Tables

Table S1. Bacterial strains and plasmids used in this study.

Strain/plasmid	Description	Source
S. enterica Typhimurium		
IR715	Nalidixic acid-derivative of ATCC 14028	[34]
FR13	IR715 *cheY*::Tn*10* (Tet^R)	[34]
FR4	IR715 tsr::pFR3 (Tet^R)	[34]
SARA1	Isolated from patient in Mexico	[74]
S. enterica Newport		
M11018046001A	Isolated from patient in PA, USA	[75]
S. enterica Enteriditis		
05E01375	Isolated from patient in PA, USA	[76]
C. koseri		
BAA-895	Human Clinical Isolate	ATCC
E. coli		
MC1655	Model of WT *E. coli*	Karen Guillemin (UO)
K12	Rosetta(DE3) BL21 derivative	Millipore Sigma
Plasmids		
pXS-sfGFP	pGEN-mcs with a modular	[65]

	sfGFP expression scaffold (Amp^R)	
pXS-mPlum	pGEN-mcs with a modular mPlum expression scaffold (Amp^R)	[65]
pET-30a(+)-*Se*TsrLBD	Vector for recombinant expression of *Se*Tsr LBD (Kan^R)	This study, Genscript
Chemicals and Recombinant Proteins		
*Se*Tsr LBD	See Method Details	This study
human serum	ISERABOTCHI100ML	Innovative Research
Deposited Data		
Crystal structure of *Se*Tsr LBD	PDB code: 8FYV	This study

Table S2. Summary of crystallographic statistics

Protein, PDB code	*Se*Tsr LBD, PDB: 8FYV
Space Group	C 1 2 1
Cell dimensions and angle (a, b, c, beta) (Å, º)	125.8, 75.2, 129.6, 116.5
Resolution (Å) [a]	58.0-2.2 (2.26-2.20)
Completeness (%) [a]	100.0 (100.0)
Total reflections	1,039,561
Unique reflections	55,162
Average I/σ [a]	7.7 (3.6)
R_{merge} [a]	0.28 (1.42)
$CC_{1/2}$ [a]	0.994 (0.838)

R_{work} (%)	24.1
R_{free} (%)	25.8
Ramachandran favored, allowed, outliers (%)	99.1, 0.9, 0.0
Protein non-hydrogen atoms	5604
Solvent atoms	283
Protein chains, residues	5, 705
Average B-factor of protein atoms ($Å^2$)	49
Average B-factor of solvent atoms ($Å^2$)	43
rms bond lengths (Å)	0.002
rms bond angles (°)	0.42

[a] Values in parentheses indicate statistics for the highest resolution shell.

Supplementary data

Data S1. Database of Tsr homologue sequences.

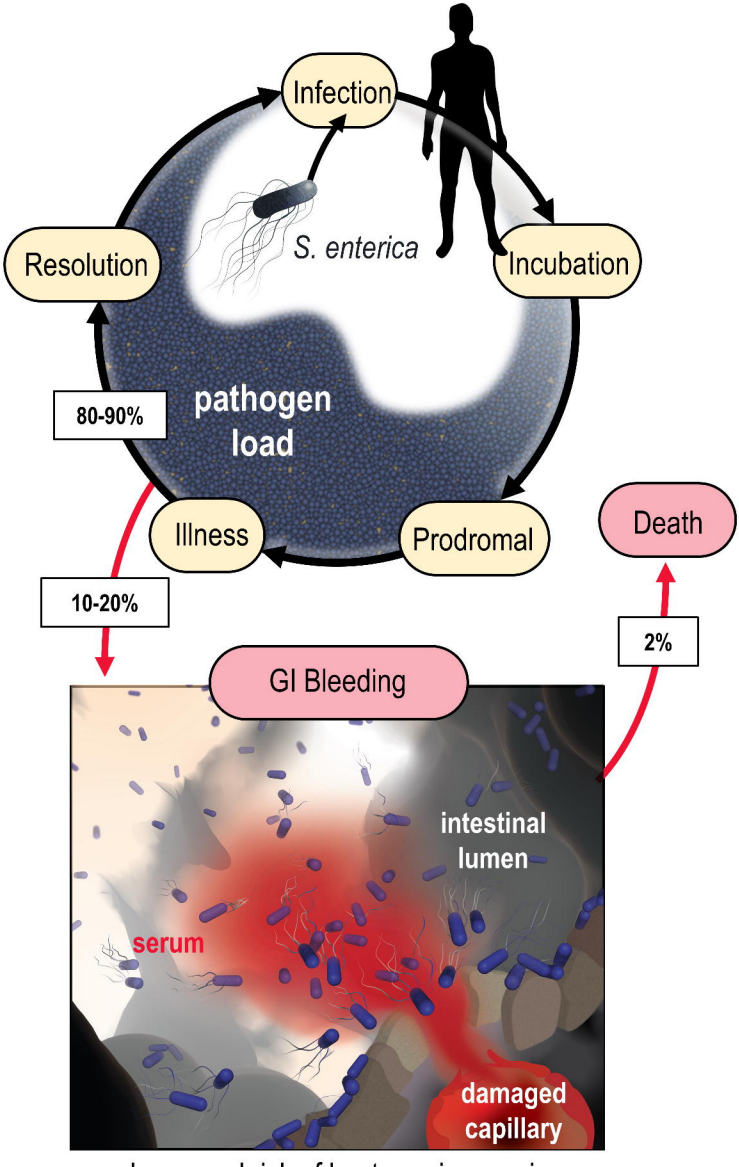
Infection
Incubation
Prodromal
Illness
Resolution
S. enterica
pathogen load
80-90%
10-20%
Death
2%
GI Bleeding
intestinal lumen
serum
damaged capillary
Increased risk of bacteremia, sepsis

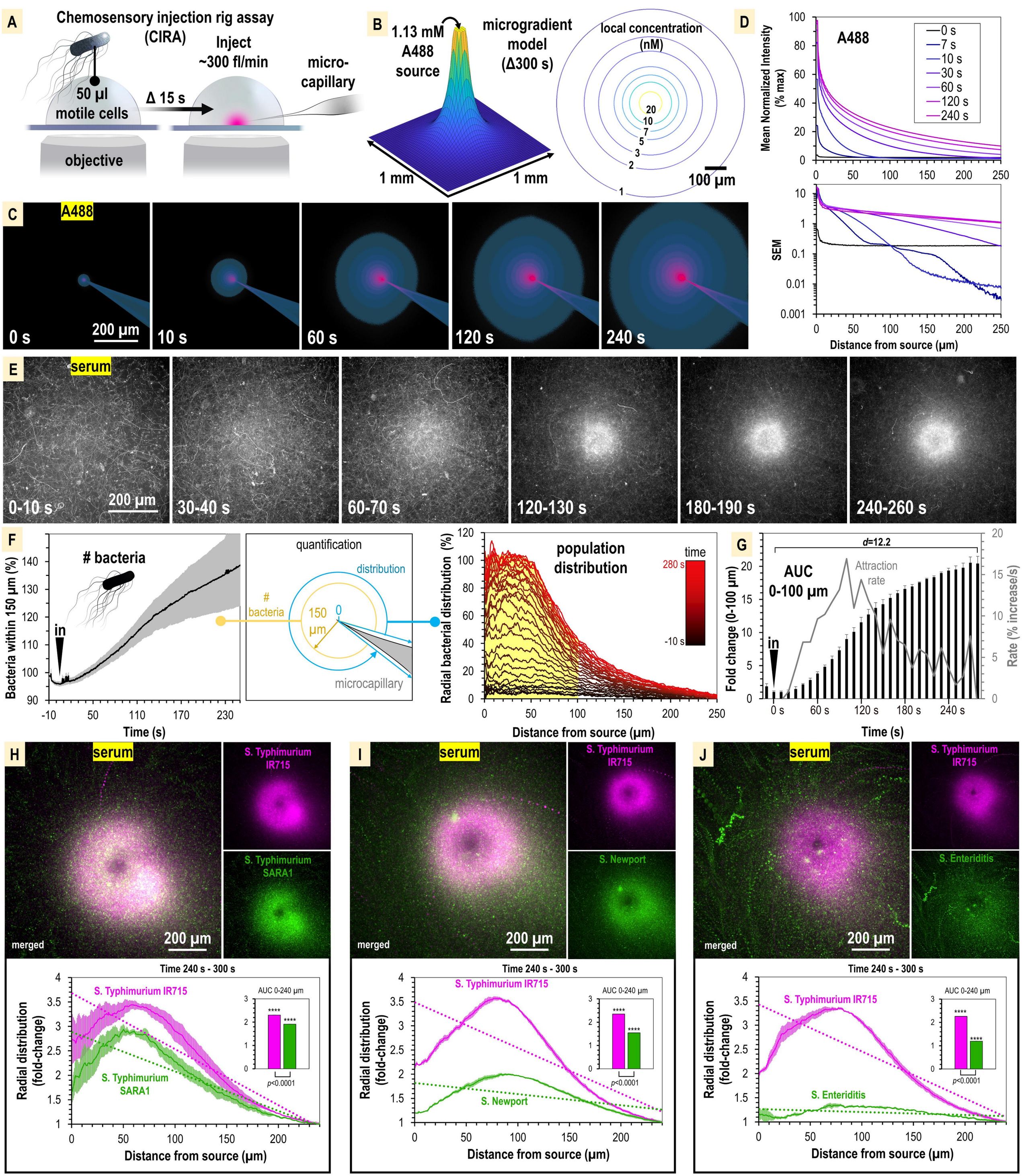
A
Chemosensory injection rig assay (CIRA)
Inject ~300 fl/min
micro-capillary
50 µl motile cells
Δ 15 s
objective
B
1.13 mM A488 source
microgradient model (Δ300 s)
local concentration (nM)
1 mm
1 mm
100 µm
C
A488
0 s
200 µm
10 s
60 s
120 s
240 s
D
A488
Mean Normalized Intensity (% max)
SEM
Distance from source (µm)
0 s
7 s
10 s
30 s
60 s
120 s
240 s
E
serum
0-10 s
200 µm
30-40 s
60-70 s
120-130 s
180-190 s
240-260 s
F
bacteria
Bacteria within 150 µm (%)
in
Time (s)
quantification
distribution
bacteria
150 µm
microcapillary
population distribution
time
280 s
-10 s
Radial bacterial distribution (%)
Distance from source (µm)
G
d=12.2
AUC 0-100 µm
Attraction rate
Fold change (0-100 µm)
Rate (% increase/s)
in
Time (s)
H
serum
S. Typhimurium IR715
S. Typhimurium SARA1
merged
200 µm
Time 240 s - 300 s
S. Typhimurium IR715
S. Typhimurium SARA1
AUC 0-240 µm
p<0.0001
Radial distribution (fold-change)
Distance from source (µm)
I
serum
S. Typhimurium IR715
S. Newport
merged
200 µm
Time 240 s - 300 s
S. Typhimurium IR715
S. Newport
AUC 0-240 µm
p<0.0001
Radial distribution (fold-change)
Distance from source (µm)
J
serum
S. Typhimurium IR715
S. Enteriditis
merged
200 µm
Time 240 s - 300 s
S. Typhimurium IR715
S. Enteriditis
AUC 0-240 µm
p<0.0001
Radial distribution (fold-change)
Distance from source (µm)

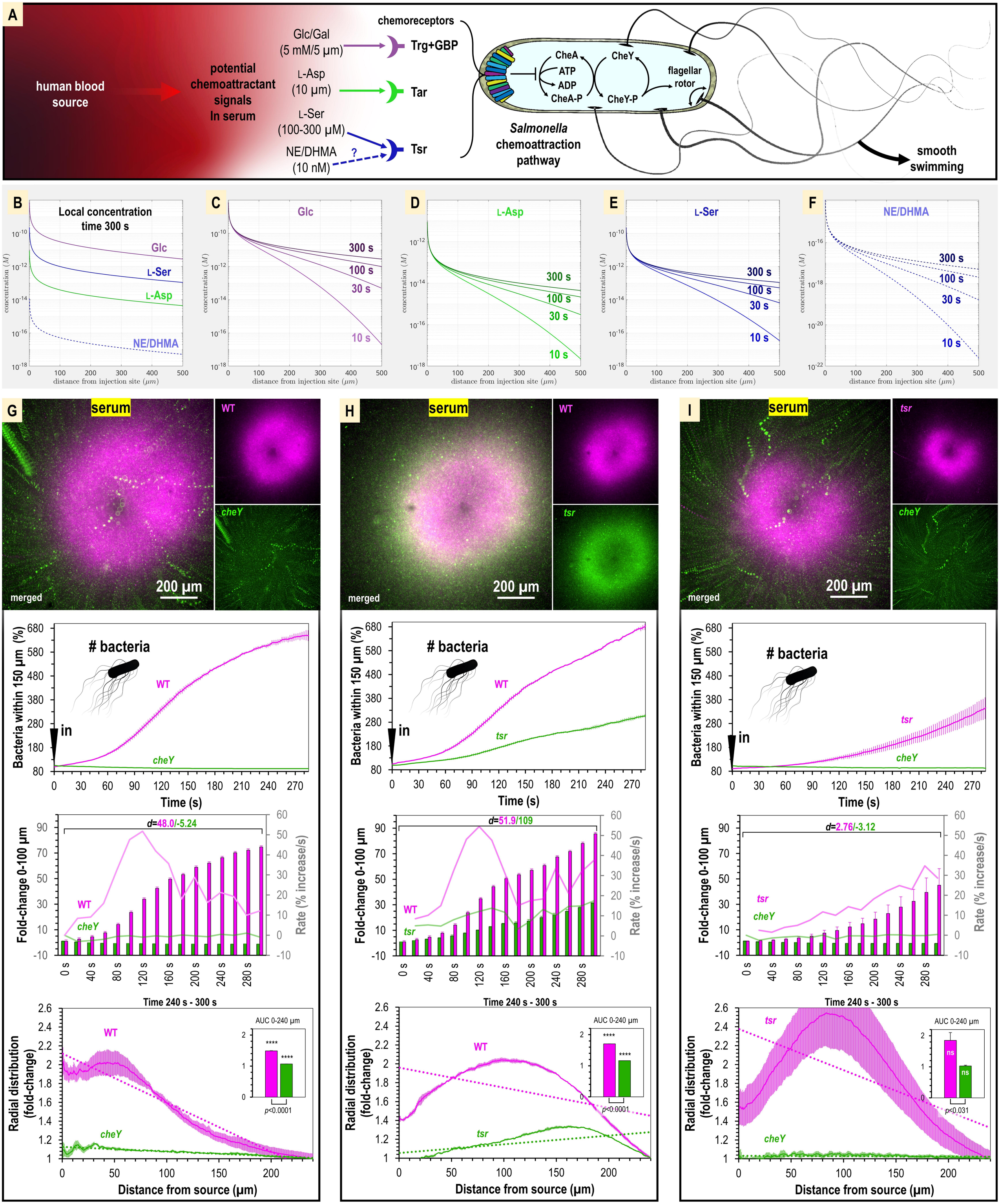
A
human blood source
potential chemoattractant signals In serum
Glc/Gal (5 mM/5 µm)
L-Asp (10 µm)
L-Ser (100-300 µM)
NE/DHMA (10 nM)
?
chemoreceptors
Trg+GBP
Tar
Tsr
CheA
ATP
ADP
CheA-P
CheY
CheY-P
flagellar rotor
Salmonella chemoattraction pathway
smooth swimming
B
Local concentration time 300 s
Glc
L-Ser
L-Asp
NE/DHMA
concentration (M)
distance from injection site (µm)
C
Glc
300 s
100 s
30 s
10 s
D
L-Asp
E
L-Ser
F
NE/DHMA
G
serum
WT
cheY
merged
200 µm
H
tsr
I
bacteria
in
Bacteria within 150 µm (%)
Time (s)
Fold-change 0-100 µm
Rate (% increase/s)
d=48.0/-5.24
d=51.9/109
d=2.76/-3.12
Time 240 s - 300 s
AUC 0-240 µm
p<0.0001
p<0.031
ns
Radial distribution (fold-change)
Distance from source (µm)

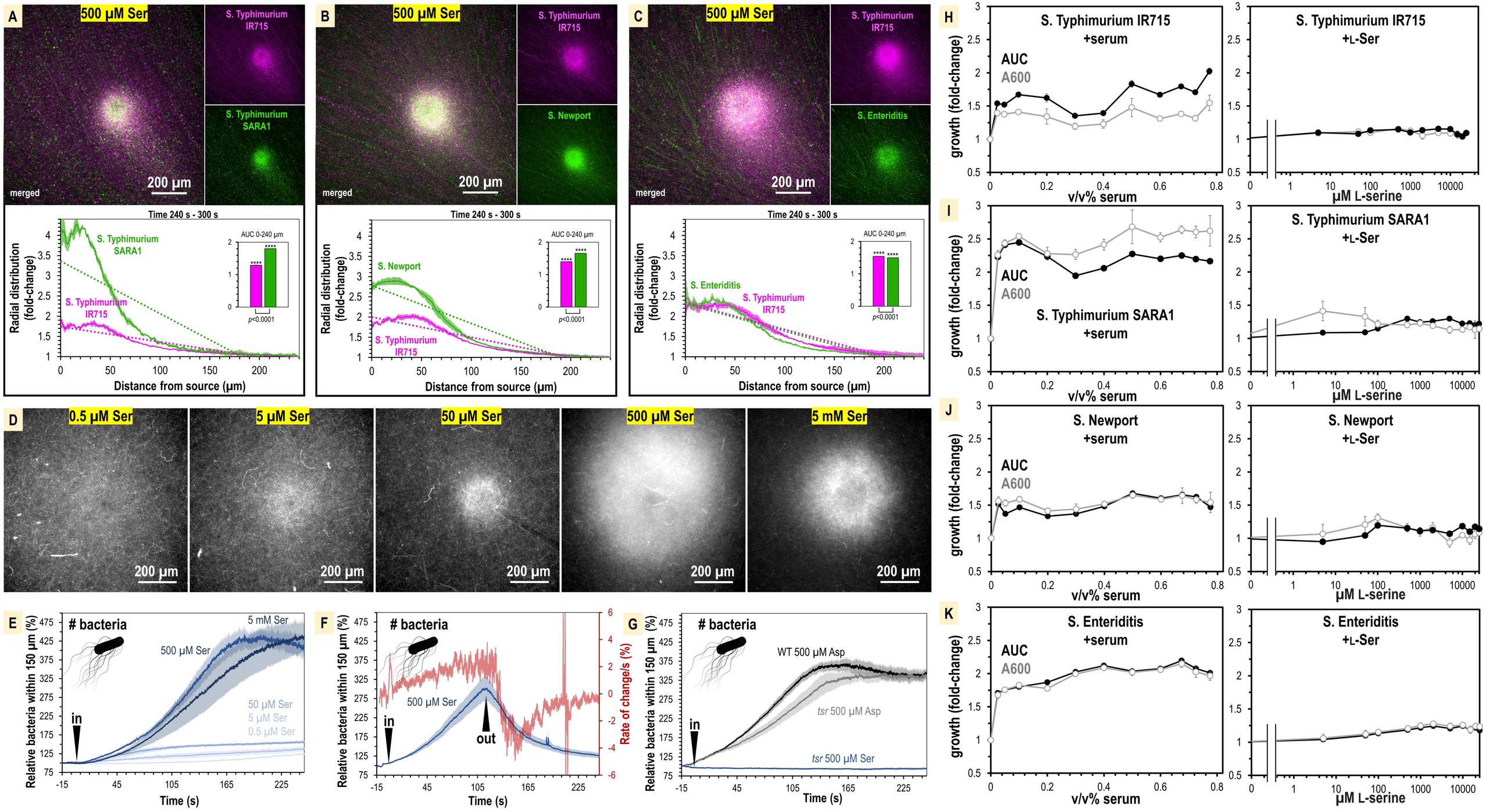
A
500 µM Ser
S. Typhimurium IR715
S. Typhimurium SARA1
merged
200 µm
Time 240 s - 300 s
Radial distribution (fold-change)
Distance from source (µm)
AUC 0-240 µm
p<0.0001
B
S. Newport
C
S. Enteriditis
D
0.5 µM Ser
5 µM Ser
50 µM Ser
500 µM Ser
5 mM Ser
E
bacteria
Relative bacteria within 150 µm (%)
Time (s)
in
F
out
Rate of change/s (%)
G
WT 500 µM Asp
tsr 500 µM Asp
tsr 500 µM Ser
H
S. Typhimurium IR715 +serum
S. Typhimurium IR715 +L-Ser
AUC
A600
growth (fold-change)
v/v% serum
µM L-serine
I
S. Typhimurium SARA1 +serum
S. Typhimurium SARA1 +L-Ser
J
S. Newport +serum
S. Newport +L-Ser
K
S. Enteriditis +serum
S. Enteriditis +L-Ser

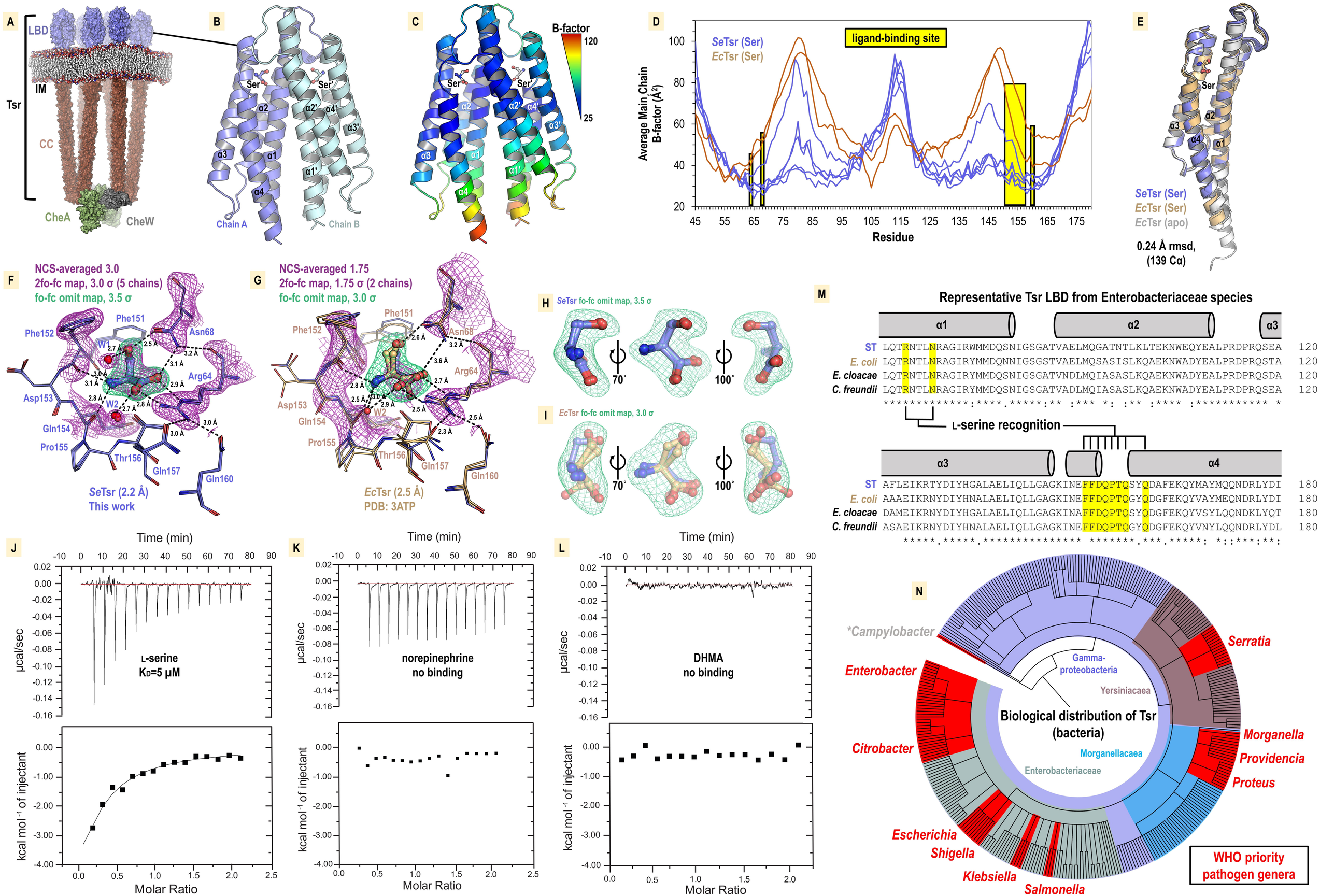
A
LBD
IM
Tsr
CC
CheA
CheW
B
Ser
Ser'
α2
α2'
α4'
α3'
α3
α1
α1'
α4
Chain A
Chain B
C
B-factor
120
25
D
SeTsr (Ser)
EcTsr (Ser)
ligand-binding site
Average Main Chain B-factor (Å²)
Residue
E
SeTsr (Ser)
EcTsr (Ser)
EcTsr (apo)
0.24 Å rmsd, (139 Cα)
F
NCS-averaged 3.0
2fo-fc map, 3.0 σ (5 chains)
fo-fc omit map, 3.5 σ
Phe151
Phe152
Asn68
Arg64
Asp153
Gln154
Pro155
Thr156
Gln157
Gln160
SeTsr (2.2 Å)
This work
G
NCS-averaged 1.75
2fo-fc map, 1.75 σ (2 chains)
fo-fc omit map, 3.0 σ
EcTsr (2.5 Å)
PDB: 3ATP
H
SeTsr fo-fc omit map, 3.5 σ
70˚
100˚
I
EcTsr fo-fc omit map, 3.0 σ
M
Representative Tsr LBD from Enterobacteriaceae species
α1
α2
α3
α4
ST LQTRNTLNRAGIRWMMDQSNIGSGATVAELMQGATNTLKLTEKNWEQYEALPRDPRQSEA 120
E. coli LQTRNTLNRAGIRYMMDQNNIGSGSTVAELMQSASISLKQAEKNWADYEALPRDPRQSTA 120
E. cloacae LQTRNTLNRAGIRYMMDQSNIGSGATVNDLMQIASASLKQAEKNWADYEALPRDPRQSDA 120
C. freundii LQTRNTLNRAGIRYMMDQSNIGSGATVADLMQIASASLKQAEKNWADYEALPRDPRQSEA 120
L-serine recognition
ST AFLEIKRTYDIYHGALAELIQLLGAGKINEFFDQPTQSYQDAFEKQYMAYMQQNDRLYDI 180
E. coli AAAEIKRNYDIYHNALAELIQLLGAGKINEFFDQPTQGYQDGFEKQYVAYMEQNDRLYDI 180
E. cloacae DAMEIKRNYDIYHGALAELIQLLGAGKINAFFDQPTQSYQDGFEKQYVSYLQQNDKLYQT 180
C. freundii ASAEIKRNYDIYHNALAELIQLLGAGKINEFFDQPTQGYQDGFEKQYVNYLQQNDRLYDL 180
J
Time (min)
μcal/sec
L-serine
KD=5 μM
kcal mol⁻¹ of injectant
Molar Ratio
K
norepinephrine
no binding
L
DHMA
no binding
N
*Campylobacter
Enterobacter
Citrobacter
Escherichia
Shigella
Klebsiella
Salmonella
Serratia
Morganella
Providencia
Proteus
Gamma-proteobacteria
Yersiniacaea
Morganellacaea
Enterobacteriaceae
Biological distribution of Tsr (bacteria)
WHO priority pathogen genera

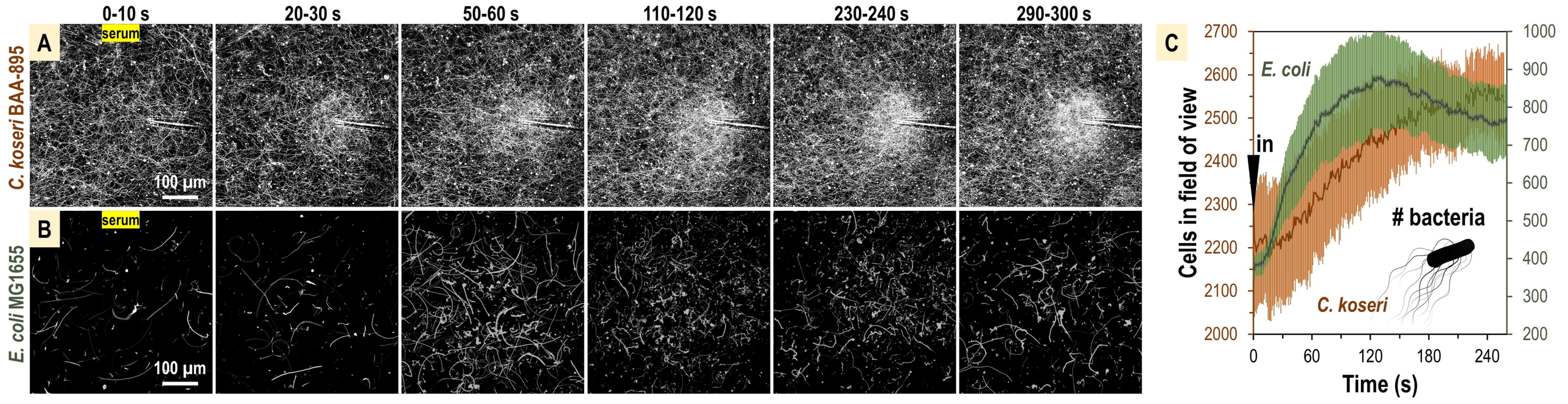
0-10 s
20-30 s
50-60 s
110-120 s
230-240 s
290-300 s
A
serum
100 µm
C. koseri BAA-895
B
serum
100 µm
E. coli MG1655
C
E. coli
in
bacteria
C. koseri
Cells in field of view
Time (s)
2700
2600
2500
2400
2300
2200
2100
2000
1000
900
800
700
600
500
400
300
200
0
60
120
180
240